CANCER IMMUNOLOGY

Bone marrow breakout lesions act as key sites for tumor-immune cell diversification in multiple myeloma

Raphael Lutz[1,2,3]†, Alexandra M. Poos[1,4]†, Llorenç Solé-Boldo[5,6,7,8]†, Lukas John[1,4]†, Johanna Wagner[9,10], Nina Prokoph[1,4], Marc A. Baertsch[1,4], Dominik Vonficht[2,3], Subarna Palit[5,6,7], Alexander Brobeil[11,12], Gunhild Mechtersheimer[11], Nina Hildenbrand[13], Stefan Hemmer[13], Simon Steiger[14], Sabrina Horn[5,15], Wojciech Pepke[13], David M. Spranz[13], Christoph Rehnitz[16], Pooja Sant[17], Jan-Philipp Mallm[17], Mirco J. Friedrich[1], Philipp Reichert[1], Stefanie Huhn[1], Andreas Trumpp[2,3,18], Karsten Rippe[14], Laleh Haghverdi[6], Stefan Fröhling[9,10,18,19], Carsten Müller-Tidow[10,20], Daniel Hübschmann[2,18,21], Hartmut Goldschmidt[1,22], Gerald Willimsky[5,15,23,24], Sandra Sauer[1], Marc S. Raab[1,4], Simon Haas[5,6,7,8,23]*, Niels Weinhold[1,4]*

The bone marrow microenvironment plays a crucial role in the development of multiple myeloma. As the disease progresses, malignant myeloma cells can evolve to survive outside the bone marrow. However, the processes underlying bone marrow independence and their consequences for immune control remain poorly understood. Here, we conducted single-cell and spatial multiomics analyses of bone marrow–confined intramedullary disease and paired breakout lesions that disrupt the cortical bone. These analyses revealed a distinct cellular microenvironment and architectural features of breakout lesions, characterized by extensive areas of malignant plasma cells interspersed with lesion-specific solitary natural killer and macrophage populations, as well as focal accumulations of immune cell agglomerates. Within these agglomerates, spatially confined T cell clones expanded alongside various immune cells, coinciding with the local genomic evolution of tumor cells. These analyses identify breakout lesions as a hotspot for tumor-immune cell interactions and diversification, representing a key event in myeloma pathogenesis.

INTRODUCTION

Multiple myeloma (MM) is a monoclonal plasma cell malignancy that remains fatal for most patients despite new treatment options (1). Typically, malignant plasma cells expand almost exclusively in the bone marrow (BM) (2). In the precursor stages of MM, diffuse BM infiltration is the predominant growth pattern of malignant cells (3, 4). In contrast, the formation of nodular accumulations of tumor cells, known as focal lesions, is closely correlated with the onset of symptomatic disease and is observed in most patients with MM (3–6). As the disease progresses, MM cells from focal lesions may disrupt the cortical bone and grow as soft tissue masses adjacent to the bone, also known as breakout lesion or paramedullary disease. An even more advanced stage is extramedullary disease (EMD), in which the malignant tissue expands outside of the skeletal system (7). In patients

treated with novel immunotherapies, the presence of EMD has emerged as one of the most important prognostic markers (8), highlighting the loss of BM dependence as a feature of advanced, aggressive disease. However, BM-independent MM cells from end-stage patients usually fail to expand in vitro, suggesting a persistent dependence on interactions with cellular and noncellular components of the tumor microenvironment (TME) (9).

Data from preclinical models support a critical role of the TME in extramedullary spread (10). However, the early processes associated with BM independence in human disease and its implications for immune control remain poorly understood. With the hypothesis that focal lesions represent an intermediate stage toward EMD, we recently performed single-cell sequencing of paired samples from diffusely infiltrated random BM (rBM) sites in the pelvis and intramedullary

[1]Heidelberg Myeloma Center, Department of Internal Medicine V, Heidelberg University Hospital, Medical Faculty, Heidelberg University, Heidelberg, Germany. [2]Heidelberg Institute for Stem Cell Technology and Experimental Medicine (HI-STEM), Heidelberg, Germany. [3]Division of Stem Cells and Cancer, German Cancer Research Center (DKFZ), Heidelberg, Germany. [4]Clinical Cooperation Unit Molecular Hematology/Oncology, Department of Internal Medicine V, Heidelberg University Hospital, Heidelberg University and German Cancer Research Center (DKFZ), Heidelberg, Germany. [5]Berlin Institute of Health (BIH) at Charité Universitätsmedizin Berlin, Berlin, Germany. [6]Berlin Institute for Medical Systems Biology, Max Delbrück Center for Molecular Medicine in the Helmholtz Association, Berlin, Germany. [7]Department of Hematology, Oncology and Tumor Immunology, Charité University Medicine, Berlin, Germany. [8]Precision Healthcare University Research Institute, Queen Mary University of London, London, UK. [9]Division of Translational Medical Oncology, German Cancer Research Center (DKFZ), Heidelberg, Germany. [10]National Center for Tumor Diseases (NCT), NCT Heidelberg, a partnership between DKFZ and Heidelberg University Hospital, Heidelberg, Germany. [11]Department of Pathology, Heidelberg University Hospital, Medical Faculty, Heidelberg University, Heidelberg, Germany. [12]Tissue Bank of the National Center for Tumor Diseases (NCT) Heidelberg, Heidelberg, Germany. [13]Department of Orthopaedics, Heidelberg University Hospital, Medical Faculty, Heidelberg University, Heidelberg, Germany. [14]Division of Chromatin Networks, German Cancer Research Center (DKFZ) and BioQuant, Heidelberg, Germany. [15]Institute of Immunology, Charité-Universitätsmedizin Berlin, corporate member of Freie Universität Berlin and Humboldt-Universität zu Berlin, Berlin, Germany. [16]Department of Radiology, Heidelberg University Hospital, Medical Faculty, Heidelberg University, Heidelberg, Germany. [17]Single Cell Open Lab, German Cancer Research Center (DKFZ), Heidelberg, Germany. [18]German Cancer Consortium (DKTK), Heidelberg, Germany. [19]Institute of Human Genetics, Heidelberg University, Heidelberg, Germany. [20]Department of Internal Medicine V, Heidelberg University Hospital, Medical Faculty, Heidelberg University, Heidelberg, Germany. [21]Computational Oncology, Molecular Precision Oncology Program, National Center for Tumor Diseases (NCT) Heidelberg and German Cancer Research Center (DKFZ), Heidelberg, Germany. [22]GMMG-Study Group at Heidelberg University Hospital, Department of Internal Medicine V, Heidelberg University Hospital, Medical Faculty, Heidelberg University, Heidelberg, Germany. [23]German Cancer Consortium (DKTK), partner site Berlin, Berlin, Germany. [24]German Cancer Research Center (DKFZ), Heidelberg, Germany.
*Corresponding author. Email: niels.weinhold@med.uni-heidelberg.de (N.W.); simon.haas@bih-charite.de (S. Ha.)
†These authors contributed equally to this work.

(BM-confined) lesions (*11*). Although modest tumor load–dependent changes in the TME were noted, no site-specific immune responses were detected in intramedullary focal lesions, although the MM cells in these lesions exhibited distinct mutational profiles. A possible explanation may be that intramedullary lesions are still dependent on the BM niche and directly exposed to its unique regulatory immune environment, dominated by immature immune and memory cells (*12, 13*). In contrast, MM soft tissue masses arising from bone lesions that disrupt the cortical bone, which are observed in 15 to 20% of patients with newly diagnosed MM (NDMM), appear to be able to survive outside the BM and may be less exposed to the immunoregulatory BM niche (*7, 14*). However, the cellular and spatial architecture of these breakout lesions, their function in tumor immunology, and their overall role in MM pathogenesis remain poorly understood.

To elucidate the early processes associated with BM independence, we dissected the cellular, immunological, and spatial ecosystem of breakout lesions from patients with NDMM. Our results show that breakout lesions are sites of bidirectional tumor-immune interactions. They consist of extensive areas dominated by MM cells and largely devoid of immune cells, with the exception of interspersed macrophages and natural killer (NK) cells with distinct transcriptional profiles. Focal accumulations of immune cells were observed within the tumor-dominated areas, typically associated with blood vessels. Such "immune islands" are active sites for tumor–T cell interactions, leading to site-enriched clonal T cell expansion and potential immune exhaustion. Collectively, these data highlight the importance of breakout lesions as key sites for tumor-immune interactions, with implications for understanding the processes underlying tumor cell dissemination and therapeutic strategies in the treatment of MM.

RESULTS
MM breakout lesions harbor a distinct cellular ecosystem
To systematically elucidate the cellular composition of MM breakout lesions, we first used a data-driven 23-plex cytometry approach (*15*), designed to quantitatively map all major BM-resident cell types ("identity panel"; table S1). Using this approach, we analyzed enzymatically digested breakout lesions and BM-confined intramedullary lesions from 11 and 5 patients with NDMM, respectively (Fig. 1A; fig. S1, A and B; and data file S1). To enable comparative analyses, we included paired samples of digested trephine biopsies (rBM stamps, $n = 16$), liquid aspirates from diffusely infiltrated rBM sites at the iliac crest (rBM Asp, $n = 8$), and peripheral blood (PB, $n = 14$) (data file S2). After batch correction, data integration, and cell type annotation, we obtained a quantitative representation of 7,609,355 high-quality cells across all samples, representing 54 ecosystems (Fig. 1B and fig. S1, C to G). These encompassed 24 cell types, including various B cell, T cell, NK cell, myeloid, plasma cell, hematopoietic stem and progenitor, stromal, and endothelial cell subsets (data file S3).

As expected, plasma cell levels gradually increased from PB to rBM and BM-confined intramedullary lesions, peaking in breakout lesions with a mean infiltration of 89.8% (range: 54.7 to 98.2%) (Fig. 1C). Compared with rBM, the B cell lineage markers CD19 and CD27 were significantly down-regulated in plasma cells from breakout lesions, whereas CD16 and the adhesion molecule CD56 were up-regulated (fig. S2, A and B, $P < 0.05$), suggesting an adapted

immunophenotype of the tumor cells in breakout lesions. In contrast, plasma cells from intramedullary lesions did not display differences compared to their rBM counterparts (fig. S2, A and B). In line with this, whole-genome sequencing (WGS) revealed a more pronounced degree of spatial subclonal heterogeneity in breakout lesions compared with intramedullary lesions, relative to their corresponding rBM pairs ($P = 0.04$; fig. S2, C and D). However, no consistent differences in cytogenetic risk were identified between breakout lesions, intramedullary lesions, and their respective paired rBM (data file S1).

To investigate the TME in detail, we excluded plasma cells from further analysis. Principal components analysis (PCA) considering cellular compositions revealed that breakout lesions harbored a TME distinct from their paired rBM samples and intramedullary lesions (Fig. 1D and fig. S3). In line with this, major cellular shifts were observed in a variety of cell types (Fig. 1, E to G). For example, breakout lesions contained considerably higher numbers of mesenchymal stromal cells and endothelial cells when compared with rBM samples, suggesting a stromal environment with high vascularization (Fig. 1, E and F). In contrast, stem and progenitor populations were largely underrepresented in breakout lesions compared with all types of BM samples, indicating that these regions play a less active role in hematopoiesis. The TME of breakout lesions was highly enriched in NK cells, which displayed a strong shift toward an inflammatory CD56^{bright} phenotype (Fig. 1G). Similarly, monocyte subsets showed an adopted phenotype, with a major shift toward CD16 expression (Fig. 1G).

Next, we investigated the abovementioned samples using a 23-plex T cell panel, designed to explore the T cell landscape in detail (table S2). This uncovered 16 T cell subsets across 1,352,284 high-quality T cells, including CD4 and CD8 naïve, memory, effector, and tissue-resident T cells, regulatory T cells (T_{regs}), and gamma-delta (gd) T cells (Fig. 1H and fig. S4). PCA demonstrated a distinct T cell landscape in breakout lesions compared with intramedullary lesions, rBM, and PB (Fig. 1I and fig. S3B). In particular, breakout lesions were depleted of CD4 and CD8 naïve and memory T cells and showed a strong enrichment of programmed death protein 1 (PD-1)[+] CD4 T cells, tissue-resident CD4 T cells, CD38^{+} gd T cells, and T_{regs} (Fig. 1, J to L, and fig. S4E). Most notably, a CD8 T cell cluster characterized by high expression of the exhaustion and checkpoint molecules CD39 and PD-1 was almost exclusively detectable in breakout lesions. Together, these data demonstrate that breakout lesions harbor a cellular ecosystem that is distinct from those of intramedullary focal lesions and diffusely infiltrated rBM.

Altered niche in breakout lesions confers reduced hematopoiesis-supporting capacity and active vascularization
To further elucidate cellular features of resident cells in breakout lesions, we performed single-cell proteogenomics [Cellular Indexing of Transcriptomes and Epitopes by sequencing (CITE-seq)] of flow cytometry–enriched cell types of interest, such as plasma cells, myeloid, NK, and T cells, as well as mesenchymal stromal and endothelial cells from five breakout lesions and matched rBM samples, resulting in 13,057 plasma cells and 39,552 high-quality TME cells (Fig. 2A, fig. S5, table S3, and data file S3).

Breakout lesions develop from BM-confined lesions by disruption of the cortical bone, followed by the outgrowth of malignant cells in soft tissue masses. Here, we investigated the potential role of
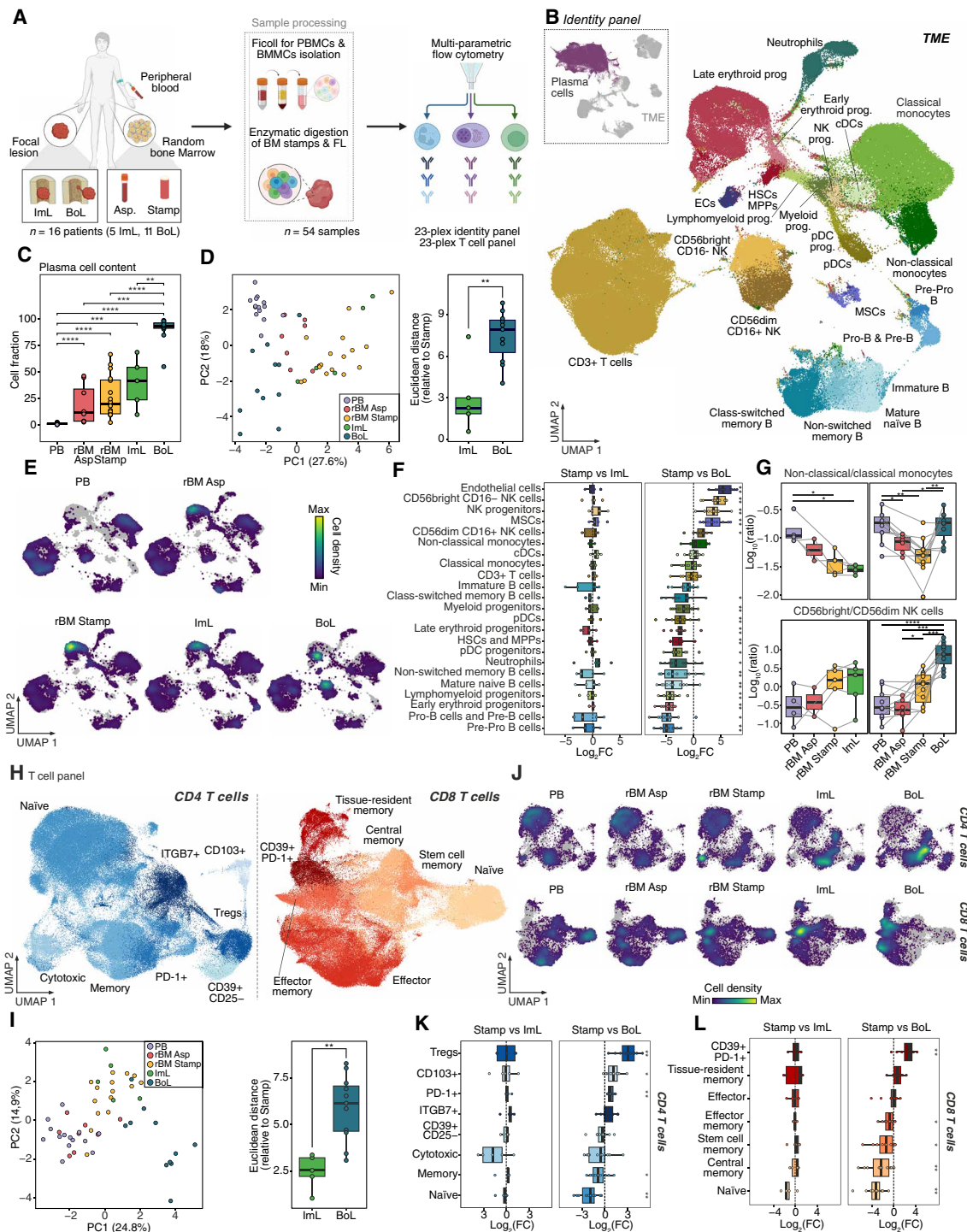
Fig. 1. Cellular ecosystem of focal lesions and paired random bone marrow in NDMM. (**A**) Experimental design. Fifty-four matched samples from 16 patients with NDMM, including 14 PB, 8 rBM aspirates, 16 rBM trephine biopsies (stamps), 5 intramedullary lesions (ImL), and 11 breakout lesions (BoL), analyzed using two 23-plex cytometry panels. PBMC/BMMC, PB or BM mononuclear cells. (**B**) Uniform manifold approximation and projection (UMAP) of identity panel data: all cell types (top) and recalculated data after exclusion of plasma cells (bottom). (**C**) Plasma cell content across samples. (**D**) PCA of cell type fractions, excluding plasma cells (left) and Euclidean distance of ImL and BoL to respective paired rBM (right). (**E**) UMAP depicting cellular density (plasma cells excluded) across sample types. (**F**) Differential cell type abundance of TME cell types between ImL or BoL and paired rBM stamps, shown as log$_2$[fold change (FC)]. (**G**) Cell fraction ratios: nonclassical/classical monocytes (top) and CD56^{bright}/CD56^{dim} NK cells (bottom) across sample types. Patients are separated by focal lesion type (ImL versus BoL). (**H**) UMAP of T cell panel data for CD4 (left) and CD8 (right) T cells across all sample types. (**I**) PCA of all identified T cell subtype fractions (left) and Euclidean distance of ImL and BoL to paired rBM stamps (right). (**J**) UMAP depicting cellular density for CD4 (top) and CD8 (bottom) T cells across sample types. (**K** and **L**) Differential abundance of CD4 (K) and CD8 (L) subtypes between ImL or BoL and paired rBM stamps, shown as log$_2$(FC). Statistical analyses: Wilcoxon tests, unpaired in (C), (D), (G), and (I) and paired in (F), (G), (K), and (L). *$P < 0.05$; **$P < 0.01$; ***$P < 0.001$; ****$P < 0.0001$.
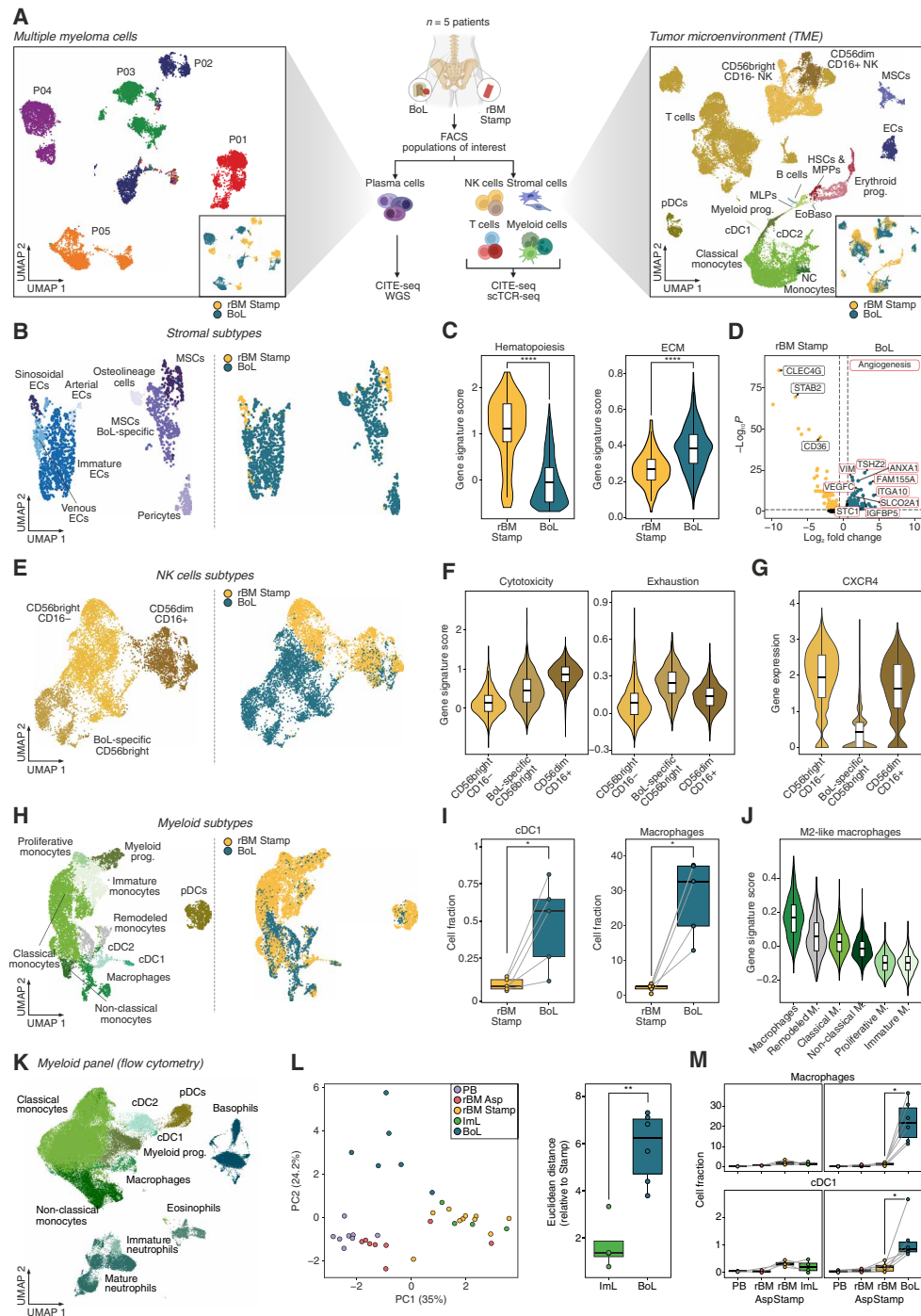
Fig. 2. Cell states in breakout lesions. (**A**) Experimental design for in-depth characterization of BoL and paired rBM stamps from five patients. Cell types of interest were sorted and analyzed using whole-genome sequencing and/or CITE-seq combined with TCR-seq. UMAP of tumor (left) and microenvironment (right) CITE-seq data are depicted. EoBaso, eosinophil/basophil/mast cell progenitors; MLPs, lymphomyeloid progenitors; NC monocytes, nonclassical monocytes; scTCR-seq, single-cell TCR-seq. (**B**) UMAP of stromal and endothelial cell CITE-seq data. (**C**) Violin and box-whisker plots for expression of hematopoiesis-supporting factors and extracellular matrix production. (**D**) Volcano plot for comparison of endothelial cell gene expression in paired samples. Significantly differentially expressed genes are depicted in yellow or blue (Wilcoxon rank sum test, Benjamini-Hochberg–adjusted $P < 0.05$, ≥1.5-fold enrichment). Angiogenesis genes are highlighted in red. (**E**) UMAP of NK cell CITE-seq data. Cells are colored by subtype (left) and sample location (right). (**F** and **G**) Violin and box-whisker plots displaying cytotoxicity (*24*) and exhaustion (*23*) gene signatures and *CXCR4* expression for indicated NK cell subtypes. (**H**) UMAP of myeloid cell CITE-seq data. (**I**) Cell fractions of cDC1s and macrophages across the five patients with paired samples, considering only the myeloid compartment. (**J**) Violin and box-whisker plots showing the M2-like macrophage gene signature (*25*) for myeloid subtypes. (**K**) UMAP of flow cytometry data for myeloid cells. Data were collected for PB, rBM aspirates and stamps, and ImL and BoL from 10 patients using a designated myeloid panel. (**L**) Principal components analysis (left) and Euclidean distance of ImL and BoL to paired rBM stamps (right) based on myeloid cell type fractions. (**M**) Macrophage (top) and cDC1 (bottom) fractions across all sample types. Statistical analyses in (C), (I), and (L) and (M) were performed using the Wilcoxon test. In (I) and (M), ImL or BoL was compared with the indicated paired samples. *$P < 0.05$; **$P < 0.01$; ****$P < 0.0001$.

the nonhematopoietic niche in this process (Fig. 2, B to D). As expected, rBM stromal cells were characterized by leptin receptor (LEPR) expression and high production of hematopoiesis-supporting factors such as *CXCL12*, *KITL*, and *IL7* (*16*). In breakout lesions, most stromal cells also expressed *LEPR* but displayed a reduced production of hematopoiesis-supporting factors (Fig. 2C and fig. S6A), consistent with the impaired hematopoiesis in breakout lesions as quantified by flow cytometry (compare Fig. 1). Moreover, stromal cells in breakout lesions showed signs of increased differentiation toward the osteoblastic lineage (e.g., *RUNX2* and *SP7*) (*17*) and elevated levels of extracellular matrix production (e.g., *COL3A1* and *SPARC*) (Fig. 2C and fig. S6A).

Endothelial cells in the rBM predominantly displayed a *STAB2*-positive sinusoidal phenotype (Fig. 2D), in line with a previous report (*16*). In contrast, endothelial cells in breakout lesions were *STAB2*-negative; displayed phenotypes associated with arterial (e.g., *HEY1* and *SOX17*), venous (e.g., *SELP* and *ACKR1*), or immature (e.g., *IGFBP5*, *TSHZ2*) identities (*18*); and were characterized by the expression of genes associated with tumor angiogenesis and endothelial sprouting (e.g., *ANXA1* and *STC1*) (*19–21*) (Fig. 2, B and D, and fig. S6B), suggesting ongoing neovascularization. Arterial endothelial cells in breakout lesions produced elevated levels of *CXCL12*, potentially mediating recruitment of immune cells to these sites (*22*).

Although the described characteristic features of breakout lesion–resident stromal and endothelial cells were observed across patients, considerable interpatient heterogeneity with regard to the expression of specific gene programs was observed, likely driven by patient-specific tumor-TME interactions (fig. S6C and data file S3). In line with this, we observed a considerable site-specific modulation of transcriptomic states of malignant plasma cells across all patients (Fig. 2A), which was consistent with pronounced differences in the subclonal architecture determined by WGS (fig. S2D). Together, these results suggest an enrichment of stromal cells in breakout lesions that may contribute to the formation of soft tissue masses extruding from the bone but have a reduced capacity to support hematopoiesis. In addition, breakout lesion endothelial cells adopt phenotypes distinct from the BM and likely contribute to neovascularization.

Breakout lesions are primary sites for tumor–immune cell interactions

Next, we used our CITE-seq data to characterize the transcriptomic and immunological states acquired by NK and myeloid cells in breakout lesions. These cells displayed significant and concordant transcriptomic alterations when compared with their respective counterparts in the rBM, indicative of sustained tumor-immune interactions (Fig. 2A). In line with our cytometric analysis, we observed a remodeling of NK cells in the TME of breakout lesions, including an enrichment of CD56^{bright} NK subsets (Fig. 2E and fig. S6, D and E). A specific NK cell subset, characterized by a particularly high expression of CD56, was exclusively identified in breakout lesions (Fig. 2E and fig. S6F). Breakout lesion–specific NK cells displayed an intermediate expression of cytotoxicity-related genes, distinct transcriptional profiles for inhibitory/activating receptors, strong expression of genes associated with immunological exhaustion, and reduced *CXCR4* levels (Fig. 2, F and G, and fig. S6, D and E), phenocopying previously described changes of NK cells in solid

tumors (*23*, *24*) and suggestive of their pronounced interaction with myeloma cells.

Similar to the NK cell compartment, major alterations in the cellular composition and transcriptional states of the myeloid compartment were observed in breakout lesions. Consistent with flow cytometry, the ratio of nonclassical to classical monocytes was significantly increased in breakout lesions (fig. S6J). Because of the higher resolution of CITE-seq compared with cytometry, we observed additional changes in the cellular composition, including an enrichment of conventional type 1 dendritic cells (cDC1s) and macrophages in the TME of breakout lesions (Fig. 2I and fig. S6J). Macrophages in breakout lesions resembled well-described tumor-associated macrophages (TAMs) in solid tumors and were characterized by an M2-like phenotype (Fig. 2J and fig. S6, G to I) (*25*).

To further validate these changes in the cellular composition of the myeloid compartment, we performed cytometric ecotyping using a 23-plex myeloid-focused panel across paired samples from 10 patients, including PB, rBM (stamps and aspirates), and both breakout and intramedullary lesions (Fig. 2, K to M; fig. S7; table S4; and data file S2). This uncovered 11 subsets across 703,084 high-quality cells from 36 matched samples (Fig. 2K and fig. S7, A to C). This analysis revealed a distinct composition of the myeloid compartment in breakout lesions compared with matched rBM and intramedullary lesions (Fig. 2L and fig. S3C) and confirmed all previous findings, including the enrichment of cDC1s and macrophages in breakout lesions (Fig. 2M and fig. S7, D to F). Jointly, these data reveal a distinct immunological state of NK and myeloid cells in myeloma breakout lesions, indicative of persistent tumor–immune cell interactions.

Breakout lesions harbor a distinct T cell repertoire dominated by clonally expanded T cells

Our flow cytometry studies uncovered notable changes within the T cell compartment of breakout lesions, including a strong enrichment of CD39$^+$/PD-1$^+$ CD8 T cells (Fig. 1). CITE-seq combined with single-cell T cell receptor (TCR) sequencing (TCR-seq) revealed that breakout lesion–resident CD39$^+$/PD-1$^+$ CD8 T cells were predominantly expanded T cell clones, overexpressing a variety of additional checkpoint inhibition and exhaustion molecules, including *CTLA4*, *LAG3*, Tim3 (*HAVCR2*), *TIGIT*, and *TOX* (Fig. 3, A to D). Thus, breakout lesion–resident CD39$^+$/PD-1$^+$ CD8 T cells appear to be antigen experienced and potentially exhausted (*26*). Most expanded clones in breakout lesions did not match previously described TCRs associated with pathogen-related T cell responses, suggesting that CD39$^+$/PD-1$^+$ CD8 T cells are likely myeloma specific (fig. S6K and data file S4). In line with this, CD39$^+$/PD-1$^+$ CD8 T cells highly overexpressed a gene signature representative of neoantigen-reactive tumor-infiltrating lymphocytes in solid cancers (Fig. 3D) (*27*).

Consistent with the expansion of T cell clones and the resulting lower TCR diversity, a reduced Chao1 index was observed in TCR repertoires of breakout lesions when compared with their paired rBM counterparts (Fig. 3E). Two patients (P01 and P02) showed a particularly strong enrichment of CD39$^+$/PD-1$^+$ CD8 T cells in their breakout lesions (fig. S6L). The vast majority of these cells were expanded T cell clones that were not detectable in the paired rBM from the same patient (Fig. 3, F to H, and data file S4), suggesting site-enriched T cell responses, further highlighting breakout lesions as a key site for tumor-immune interactions.
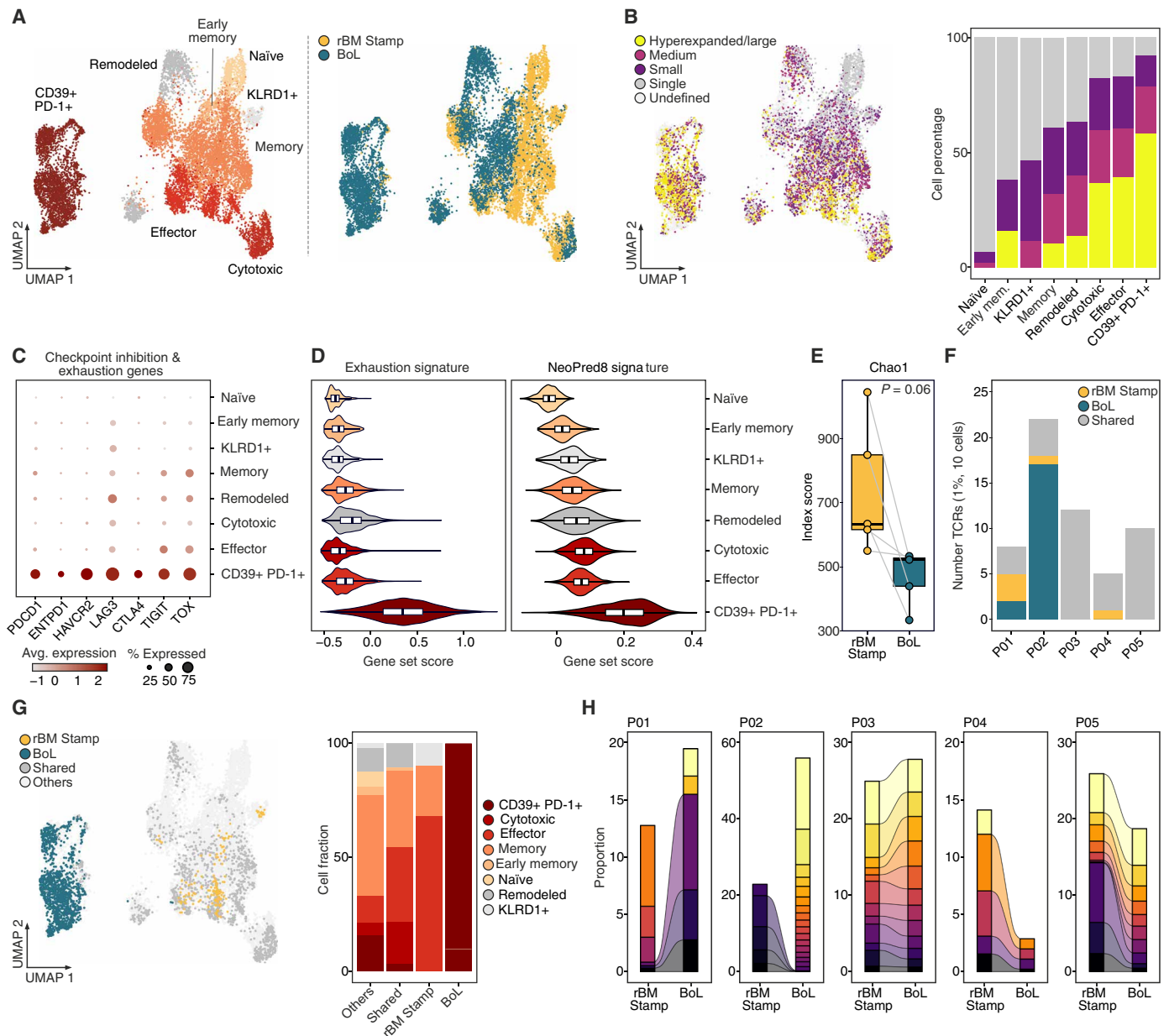
Fig. 3. T cell repertoire of breakout lesions and paired random BM. (**A**) UMAP representation of CITE-seq data for CD8 T cells from five patients with paired samples. Cells are colored by cell type (left) and sample location (right). (**B**) Left: Same UMAP as in (A) colored by the level of T cell expansion. Undefined: T cells without TCR information. Right: Proportion of expanded T cells per CD8 T cell subtype. T cells without TCR information were excluded. (**C**) Expression of immune checkpoint molecules per CD8 T cell subtype. Color and size of points indicate the average expression and the percentage of positive cells, respectively. (**D**) Violin and box-whisker plots for a T cell exhaustion signature (*28*) and a signature of neoantigen-reactive tumor-infiltrating lymphocytes from solid cancers (*27*) per CD8 T cell subtype. (**E**) T cell diversity according to the Chao1 index for BoL and paired rBM stamps. The box plots show the median and the interquartile range, whereas the upper and lower whiskers show the highest and lowest value (excluding outliers), respectively. The *P* value was calculated using the Wilcoxon signed-rank test. (**F**) Total number of T cell clones that were shared between BoL and rBM stamp (gray) or unique to either the rBM stamp (yellow) or the BoL (blue). Only T cell clones with a proportion of ≥1% and ≥ 10 cells in at least one of the paired samples were considered. (**G**) T cell clones that were unique to BoL (blue) or rBM stamps (yellow) and shared T cell clones are highlighted in the UMAP for CD8 T cells (left) and assigned to CD8 T cell subtypes (right). CD8 T cell clones with a proportion of <1% and/or <10 cells in both of the paired samples were classified as "Others." (**H**) CD8 T cell proportion of all expanded T cell clones in paired BoL and rBM stamps, considering clones with a proportion of ≥1% and ≥10 cells in at least one of the paired samples.

Spatially resolved single-cell analysis reveals microregional tumor-immune interactions

To further investigate subregion-specific tumor-immune interactions, we dissected a particularly large breakout lesion from patient P02 into 16 spatially defined microregions and performed cytometric cellular ecotyping, yielding a total of 63,671 TME cells (identity panel) and 46,442 T cells (T cell panel), and CITE-seq with paired TCR-seq, yielding 16,462 TME cells, across individual regions

(Fig. 4A and fig. S8, A and B). First, using our spatially resolved cytometry data, we determined plasma cell levels, quantified cellular abundances of the TME, and mapped T cell subsets across all regions (Fig. 4B). Although all subregions showed MM cell infiltration levels >90%, this analysis uncovered substantial spatial variation in the absolute and relative composition of immune cells, with CD39^{+}/PD-1^{+} CD8 T and CD56^{bright} NK cells being most regionally variable, suggesting differences in local hotspots of tumor-immune interactions (Fig. 4, C and D, and fig. S8A).

To investigate colocalization of immune cell types within such hotspots, we performed a correlation analysis of cellular abundances across the regions (Fig. 4E and data file S5). This revealed two major clusters, consisting of cell types quantitatively coinciding in spatial regions. Cluster 2 was predominated by immunoregulatory T$_{regs}$ and a group of T cell subtypes with an antigen-experienced phenotype, including PD-1– or CD39–expressing CD4 T cells, and the above described clonally expanded CD39^{+}/PD-1^{+} CD8 T cells, indicating a concerted immunoregulatory or antigen-experienced environment (Fig. 4E). The abundance of cluster 2 cell types generally correlated with the total amount of T cells and cDC1s, suggesting the establishment of local immunoregulatory T cell environments as a consequence of the expansion of antigen-experienced T cells (Fig. 4, E to G). In contrast, cluster 1 was associated with high plasma cell levels and the absence of T cells with an antigen-experienced phenotype. In line with this, the presence of clonally expanded CD39^{+}/PD-1^{+} CD8 T cells was anticorrelated with plasma cell counts and breakout lesion–specific NK cell subsets, indicating their spatial separation (Fig. 4, E to G).

Spatially resolved cytometry analyses from six additional patients confirmed the high degree of intralesion heterogeneity within the immune compartment of breakout lesions (fig. S8C and data file S5). For one patient with high (P11) and one patient with low (P05) levels of CD39^{+}/PD-1^{+} CD8 T cells, sufficient regions were available for correlation analysis. Although the patient with high levels of CD39^{+}/PD-1^{+} CD8 T cells (P11) showed features very similar to those of patient P02, less overall spatial heterogeneity was observed in the patient with a low number of antigen-experienced T cells (P05) (fig. S8, D and E). Together, these analyses reveal substantial regional heterogeneity in the distinct immune cell communities within breakout lesions, linked to the presence of T cells with an antigen-experienced phenotype.

Spatially separated coevolution of genomic tumor cell diversification and expanded T cell clones

To investigate potential causes underlying intralesion heterogeneity, we analyzed single-cell TCR-seq data of the spatially separated microregions of patient P02. This analysis revealed that distinct lesion-specific T cell clones were operational in separate regions within the lesion (Fig. 5, A to C; fig. S9, A and B; and data file S6). For example, the hyperexpanded T cell clone #3 dominated the adjacent regions R1 and R2 but was not observed in the distally located regions R8 to R16 (Fig. 5, A and B, and fig. S9B). Conversely, these regions harbored several expanded T cell clones (i.e., TCR clone #2 and clone #14) that were not present in regions R1 and R2 (Fig. 5, A to C, and fig. S9B).

To address the question of whether the spatial heterogeneity of clonal T cell responses might be a consequence of divergent genomic tumor evolution in distinct spatial territories of the breakout lesion, we performed WGS of MM cells from six selected regions and

from the paired rBM of patient P02 (Fig. 5, D and E, and fig. S9C). This analysis revealed gain(1q21) and $KRAS^{G12A}$ as driver events for the common ancestor at the site of the breakout lesion, which was present at the minor subclonal level in the matched rBM stamp. Within the breakout lesion we found two major evolutionary subclonal branches (Fig. 5, D and E, and fig. S9C). Branch 1, which included a $HOXD3^{E333D}$ mutation, was dominant in region R1, present at the minor subclonal level in adjacent regions R2 and R5, and barely detectable in distally located regions R10, R14, and R16 (Fig. 5D). In contrast, branch 2, which was defined by the driver event $TP53^{T284fs}$ (Fig. 5D), dominated the distally located regions R10, R14, and R16, indicating ongoing diversification and subclones under positive selection in the breakout lesion (29). The observed spatial genomic divergence coincided with the spatial heterogeneity of T cell clones (Fig. 5, B, D, and E). For instance, TCR clone #3 was exclusively present in regions enriched for tumor subclones from branch 1, whereas TCR clone #2 and #14 were enriched in regions mostly containing tumor subclones from branch 2 (Fig. 5, B, D, and E). However, some differentially enriched TCRs were also observed between regions without detectable heterogeneous mutations, e.g., regions 14 and 16, suggesting that a combination of genomic and microenvironmental factors may underlie TCR heterogeneity.

To further investigate a potential relationship between genomic diversification in tumor cells and clonal T cell expansions, we performed spatially resolved bulk WGS and TCR-seq of one to six regions of the breakout lesions and paired rBM stamps in eight additional patients, corresponding to the same patients included in the extended flow cytometry analysis (Fig. 5, F to I, and fig. S10). These analyses confirmed extensive intralesion heterogeneity at the genomic and TCR level, with enriched expanded T cell clones in breakout lesions compared with paired rBM stamps in six of eight patients (fig. S10E).

In line with the single-cell sequencing data (Fig. 3), there was a trend toward reduced TCR diversity in breakout lesions, which correlated with the fraction of CD39^{+}/PD-1^{+} CD8 T cells (fig. S10, F and G). There was also a correlation between the number of enriched TCR clones (fold change ≥ 10) and the degree of spatial subclonal tumor heterogeneity in paired comparisons between breakout lesions and rBM stamps or between regions from the same lesion, supporting an association between genomic myeloma evolution and adaptive T cell responses (fig. S10H; see Materials and Methods). These findings collectively reveal that breakout lesions are critical hubs for concurrent genomic tumor evolution and spatial diversification, likely playing a significant role in expanding the heterogeneity of antitumor immune responses.

Architectural principles of breakout lesions

Our spatially resolved analysis revealed an unbalanced distribution of immune cells across distinct subregions of breakout lesions. To further explore this phenomenon, we first performed immunohistochemistry (IHC) on 21 breakout lesions and their paired rBM stamps to identify CD8 T cells (CD8), monocytes/macrophages (CD68), and plasma cells [multiple myeloma oncogene 1 (MUM1)]. Nine of 21 breakout lesions, including those from the two patients with expanded antigen-experienced T cell clones, displayed nodal immune infiltrates surrounded by large territories dominated by plasma cells, which we termed "immune islands" and "plasma cell–dominated areas," respectively (Fig. 6A and fig. S11A). We did not observe a comparable pattern in paired rBM stamps (fig. S11B), in
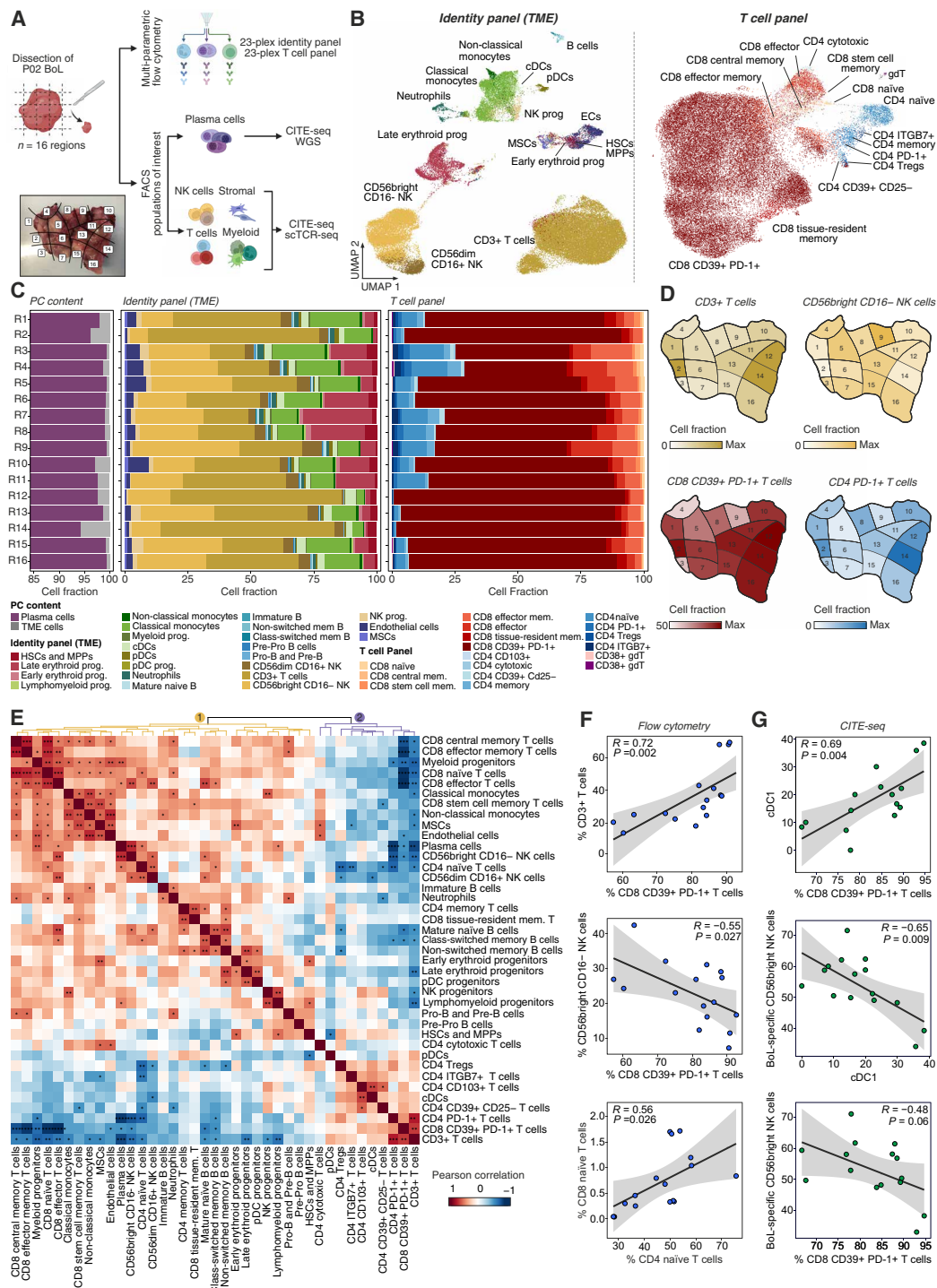
Fig. 4. Spatially resolved cellular ecotyping of a breakout lesion. (**A**) Experimental design for the analysis of 16 spatially resolved regions of the breakout lesion of patient P02 using flow cytometry, single-cell proteogenomics (CITE-seq) and V(D)J-based TCR-seq. (**B**) Left: UMAP representation of flow cytometry data collected using the identity panel including all cells from the 16 regions except for plasma cells ($n = 63,671$ cells). Right: UMAP representation of T cells analyzed with the T cell panel, including all T cells from the 16 regions ($n = 46,442$ cells). (**C**) Bar plots depicting cellular fractions for the 16 regions obtained using the identity panel (left: plasma cell count; middle: TME cell fractions) and the T cell panel (right). (**D**) Spatial distribution of selected cell types across the 16 regions. Regions are colored on the basis of relative fractions for TME cell types (top) or relative fractions from CD4 and CD8 T cell subsets (bottom). (**E**) Correlation matrix of cell fractions obtained from flow cytometry data. Plasma cell counts, relative fractions for TME cell types (identity panel), and relative fractions from CD4 and CD8 T cell subsets (T cell panel) were used. Color represents Pearson's correlation coefficient values. Statistically significant correlations are highlighted: *$P < 0.05$; **$P < 0.01$; ***$P < 0.001$; ****$P < 0.0001$. (**F**) Examples of statistically significant correlations between cell fractions from flow cytometry in the 16 regions depicted as scatterplots. (**G**) Correlations between CD39^{+}/PD-1^{+} CD8 T cells, cDC1s, and BoL-specific CD56^{bright} NK cells based on CITE-seq data for 15 of 16 regions of patient P02 depicted as scatterplots. For the calculation of cell fractions, only cells from the same cellular compartment were considered to account for the cell sorting before CITE-seq.
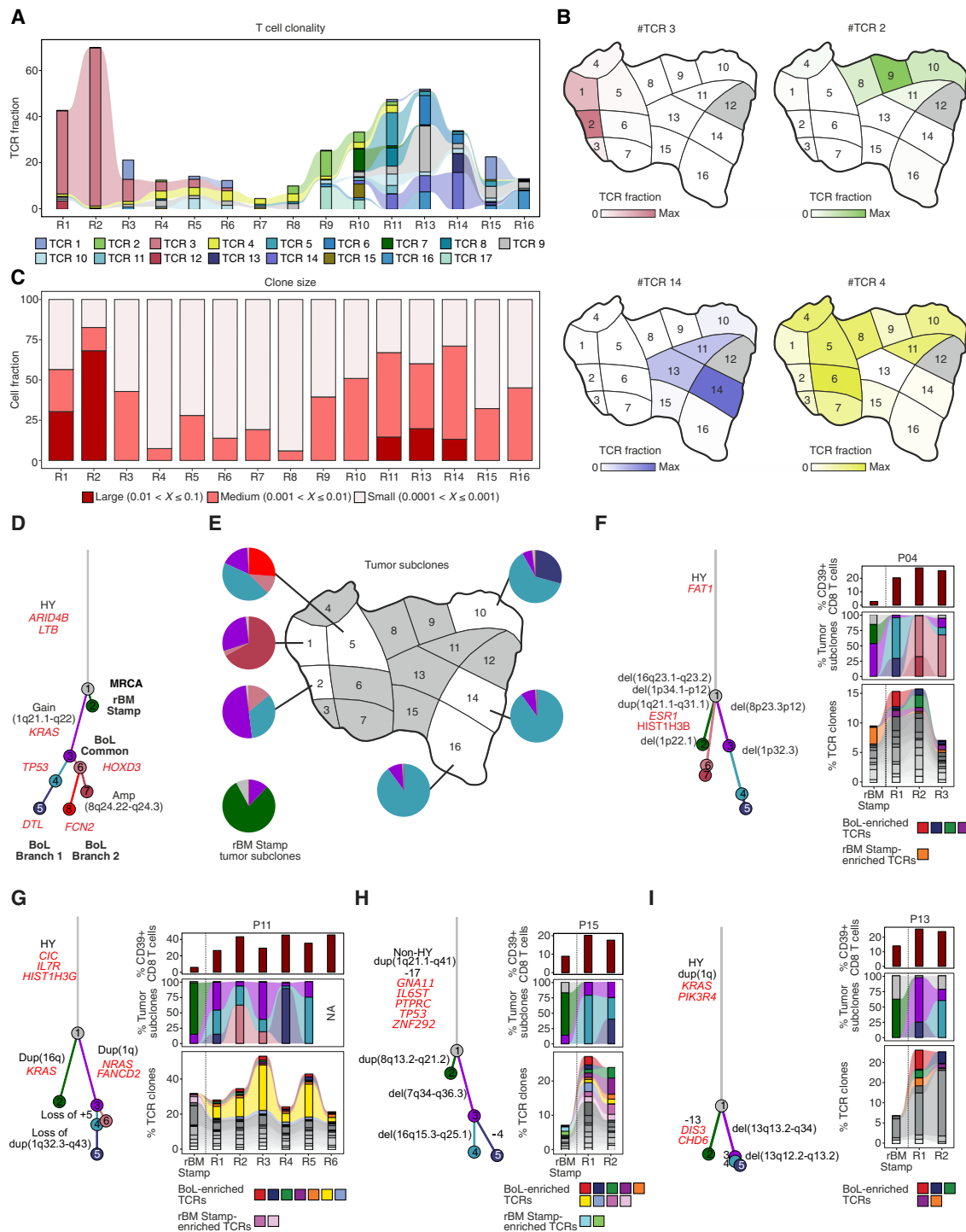
Fig. 5. Spatial distribution of T cell clones and tumor subclones within breakout lesions. (**A**) Distribution of expanded T cell clones across the BoL of patient P02 according to single-cell TCR-seq. We considered only T cell clones with at least 25 cells in at least one region, which were not detectable in the paired rBM stamp and peripheral blood. Because of insufficient sample material, CITE-seq and TCR-seq data were not available for region 12. (**B**) Spatial distribution of four selected T cell clones across the regions. Regions are colored according to the proportion of the indicated T cell clone. (**C**) Total proportion of expanded T cell clones per region. (**D**) Phylogenetic tree based on WGS data for six selected regions from the BoL (R1, R2, R5, R10, R14, and R16) and the paired rBM stamp of patient P02. Selected mutations and copy number aberrations are highlighted in red and black, respectively. HY, hyperdiploid karyotype; MRCA, most recent common ancestor. (**E**) Pie charts showing the proportion of the identified tumor subclones per region. The subclones are color-coded in line with the phylogenetic tree in (D). (**F** to **I**) Bulk WGS and TCR data for four additional patients with multiple regions per breakout lesion. Left: Phylogenetic tree. dup, chromosomal duplication; del, chromosomal deletion. Top right: Bar plots depicting the relative cell fraction of CD39+/PD-1+ CD8 T cells per sample as determined by flow cytometry. Middle right: Alluvial plot depicting the fraction of tumor subclones per region. Bottom right: Alluvial plot depicting cell fractions of expanded TCR clones (≥1% of total TCR repertoire) per region. Shared TCRs are shown in shades of gray, whereas enriched TCR clones (fold change ≥ 10) are depicted in color.

Fig. 6. Immune islands as sites of tumor-immune interactions in breakout lesions. (**A**) Multiplexed imaging of the breakout lesion of patient P02. An immune island (area 1, left) and a representative region of the surrounding plasma cell–dominated areas (area 2, right) are shown. Cells are colored according to their cell type. In the middle panel, a consecutive slide was stained for CD8 T cells using immunohistochemistry. (**B**) Location of selected cell types in the immune island (top) and the plasma cell–dominated area (bottom) with color code from (A). Except for the cell type of interest and plasma cells (blue), all other cell types were masked. The dot size of the highlighted cells has been increased to improve visibility. (**C**) Neighborhood analysis based on windows of 10 cells. The neighborhoods are shown for area 1 (left) and area 2 (right). Middle: Heatmap depicting the enrichment score for cell types within each neighborhood. The color code for the neighborhoods is shown below the heatmap. (**D**) Summary of key features observed in breakout lesions of 10 patients using multiplexed imaging data. IF, immunofluorescence. (**E**) Cellular composition of the analyzed immune islands per patient.
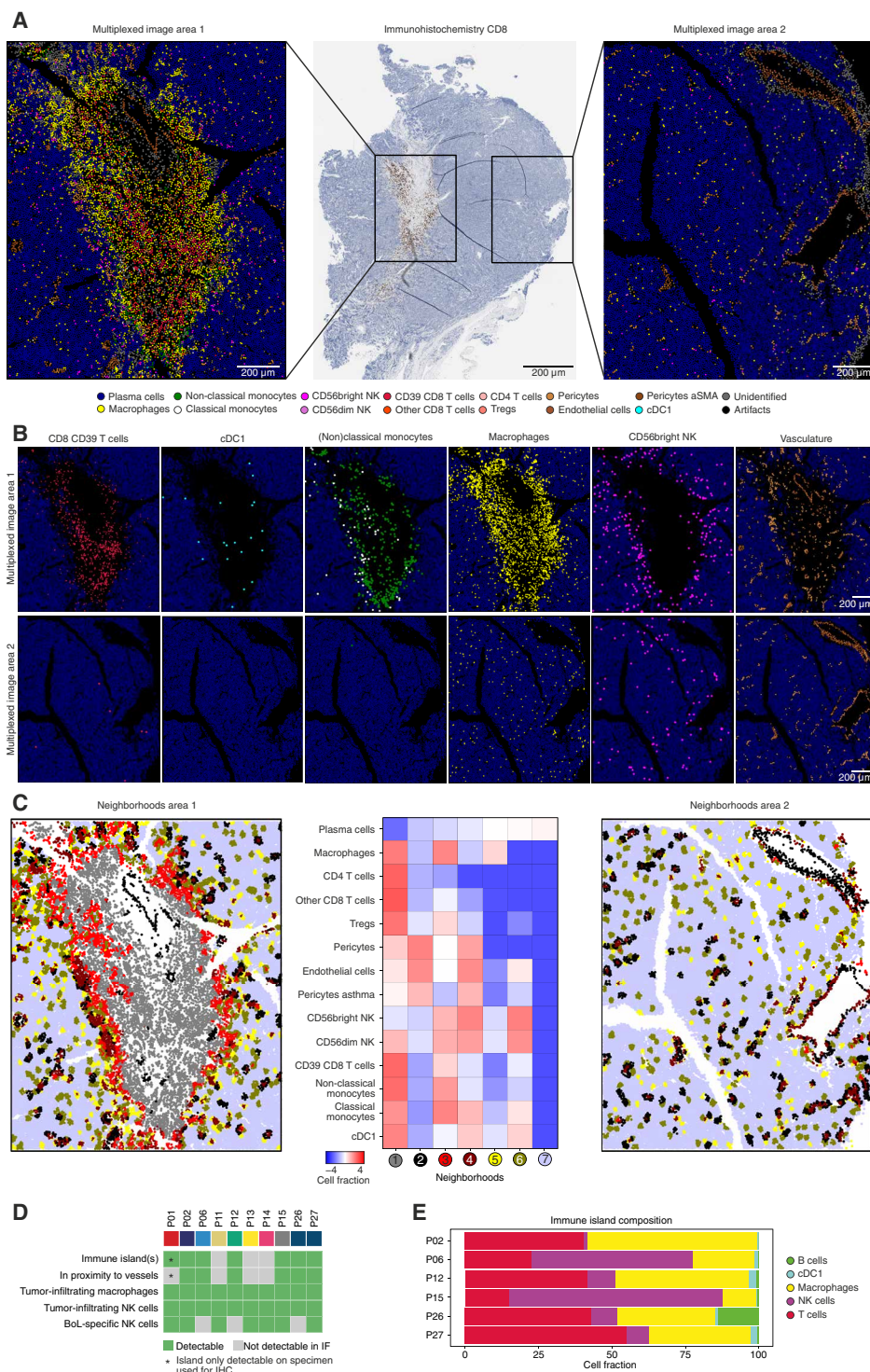
line with the distinct makeup of the immune ecosystem of breakout lesions as described throughout the manuscript.

To map the spatial architecture of immune islands and plasma cell–dominated areas in more detail, we performed highly multiplexed immunofluorescence imaging of a breakout lesion from patient P02, which included a large immune island and pronounced expansion of site-enriched T cell clones (Fig. 6). For this purpose, we designed a panel to spatially map all major cell types resident in the breakout lesion, including plasma cells, macrophages, CD56^{bright} NK cells, and CD39^{+} CD8 T cells (table S5). In total, we identified 14 distinct cell types (Fig. 6, A and B, and fig. S11C). To analyze interactions among the cell types, we calculated cellular neighborhoods (CNs), defined as regions with recurrent combinations of cell types (Fig. 6C) (30). For this purpose, we analyzed windows containing the 10 closest spatial neighbors of each cell and clustered these windows according to their cellular composition (30). In total, we defined seven CNs recapitulating different components of the immune island and the plasma cell–dominated areas.

These included the center of the immune islands (CN-1), the rim of the islands (CN-3), endothelial neighborhoods (CN-2 and CN-4), the plasma cell–dominated areas (CN-7), as well as two neighborhoods within the plasma cell–dominated areas, which showed an enrichment for macrophages (CN-5) and NK cells (CN-6), respectively. Consistent with our previous spatial analyses and IHC, CD4 and CD8 T cell subsets were almost exclusively present in the center of

the immune islands (CN-1), were depleted at island rims (CN-3), and rarely infiltrated the plasma cell–dominated areas (CN-7) (Fig. 6, A to C). Most CD8 T cells exhibited an antigen-experienced phenotype, characterized by the coexpression of CD39, LAG3, and TIM3, and were actively expanding, as indicated by Ki67 positivity (fig. S11D), in line with our flow cytometry and CITE-seq data. cDC1s were observed in close proximity to CD39^{+} CD8 T cells,

suggesting ongoing antigen presentation, further supporting a model in which immune islands in breakout lesions act as active sites of tumor-immune interactions. A large blood vessel was located at the center of the immune island, likely serving as an entry point for immune cells from the circulation. Moreover, vascular structures were frequently observed at the border between the immune island and the plasma cell–dominated areas, suggesting neovascularization as a consequence of tumor-immune interactions, in line with our single-cell data.

Myeloid cells displayed various phenotypes highly dependent on their spatial localization. Consistent with our previous analysis, nonclassical monocytes were highly enriched in the immune island and localized primarily to the island rim in close proximity to but not infiltrating the plasma cell–dominated area (Fig. 6B). Classical monocytes were less abundant and displayed a similar spatial pattern but could also be observed in or close to smaller blood vessels. In contrast, M2-like tissue-resident macrophages (CD206$^+$) not only were observed in the immune islands as well but also homogeneously infiltrated the plasma cell–dominated area (Fig. 6B and fig. S11C). Similarly, NK cells, especially CD56^{bright} NK cells with high granzyme B (GZMB) expression, migrated from the immune islands and infiltrated the plasma cell–dominated area homogeneously, in line with their lesion-specific expansion and phenotypes (Fig. 6B and fig. S11C).

We then expanded our multiplex imaging to include nine additional breakout lesions with sufficient residual material. This analysis not only confirmed several key features of breakout lesions identified in patient P02 but also revealed substantial interpatient heterogeneity (Fig. 6D). Multiplex imaging confirmed the presence of focal accumulations of immune cells detected by IHC, except in one patient (P01), where different specimens from the same lesion were used for IHC and multiplex imaging because of limited material (Fig. 6, D and E). Although the size, composition, and morphology of the immune islands varied (Fig. 6E), they consistently showed an enrichment of CD8$^+$ T cells compared with the surrounding tumor-dense areas and were located in close proximity to blood vessels (Fig. 6D and fig. S12A). Solitary tumor-infiltrating macrophages and NK cells were observed in all nine samples, and the breakout lesion–specific CD56^{bright} NK cell phenotype (CD7$^+$/CD56^{bright}/GZMB$^+$/CD16$^-$) was detected in six of them (Fig. 6D and fig. S12, B and C). These analyses demonstrate that, although there is considerable heterogeneity between breakout lesions, several key features appear to be conserved in most of them. Together, these data reveal the distinct spatial organization of MM breakout lesions, which differ markedly from their BM-confined counterparts, featuring immune cell–rich islands and plasma cell–dominated regions as major compartments. Immune islands are key sites of T cell expansion and neovascularization, whereas specific NK cell and macrophage populations are capable of infiltrating the plasma cell–dominated areas.

DISCUSSION

The BM microenvironment plays a pivotal role in the development, progression, and treatment of MM (31). However, most studies focus on samples collected from a randomly selected single site of the pelvis, regardless of regional disease evolution (6, 32). Here, we have systematically compared such pelvic samples with BM-confined (intramedullary) lesions and so-called breakout (paramedullary) lesions that disrupt the cortical bone and grow as soft tissue masses. Jointly, these analyses uncover the disruption of the cortical bone as a key event in the pathogenesis and tumor immunity of MM. Significantly, the immune and stromal compartments within breakout lesions exhibit a series of major adaptations not previously reported to this extent in MM. Several of these phenocopy features were previously recognized in solid tumors, including macrophages with hallmark traits of TAMs, such as *TREM2* and *FOLR2* expression (25, 33–35); the development of T and NK cells with an antigen-experienced phenotype (23, 36, 37); and T cells with a phenotype similar to a recently described tumor-specific T cell signature in melanoma (26). Given that these adaptations were not observed in paired BM counterparts, they are likely consequences of sustained tumor-immune interactions and changes from a medullary to a nonmedullary immune microenvironment.

Changes in the BM immune TME have recently also been reported in advanced stages of plasma cell dyscrasias, including an increase in NK cells, T_{regs}, and immunosuppressive macrophages, as well as a depletion of memory T cells in active MM compared with precursor conditions, albeit to a lesser extent (31, 38, 39). Patients with early relapse show an increase in M2 macrophages and CD8 T cells with an exhaustion signature (40), and higher levels of such CD8 T cells have recently been associated with poor response to immunotherapy (41, 42), suggesting that changes within the TME of breakout lesions are consistent with high-risk and/or treatment-resistant disease. This interpretation is supported by the recent observation that the presence of multiple breakout lesions is an independent prognostic factor in MM (14). Correlating immune parameters of breakout lesions with clinical outcome will be an important next step, but the difficulty in obtaining such samples, the limited clinical follow-up when new sample processing procedures are applied, and the presence of potential confounders such as subclonal heterogeneity within breakout lesions make such an analysis challenging.

Spatial analysis revealed that the organizational principles of breakout lesions differ drastically from BM sites, with a diffuse infiltration pattern, with immune islands and plasma cell–dominated areas often dominating the breakout lesion landscape. Immune islands are sites of immune cell expansion and interaction with malignant plasma cells surrounding the immune islands in tumor cell–dominated areas. Although immune islands resemble tertiary lymphoid organs observed in solid tumors (43) to some extent, they were devoid of B cells and dominated by T, NK, and myeloid cells. Immune islands typically formed around blood vessels and contained cDC1s, in line with recent findings that these cells promote the infiltration of antigen-specific T cells in MM and other tumors (44, 45). In contrast with T cells, monocytes, and dendritic cells, which were mainly observed within the immune islands, distinct populations of NK cells and macrophages were capable of homogeneously infiltrating the plasma cell–dominated areas. However, their exact role in myeloma pathogenesis and immune regulation remains to be clarified.

Our data suggest that breakout lesions may be a hotspot for subclonal evolution that likely drives diversification of the T cell repertoire. Therefore, breakout lesions may play a key role in both the generation of tumor heterogeneity and T cell immune responses. However, in addition to genomic events, micro- and macroenvironmental factors may also contribute to the differential immune cell responses in breakout lesions. Putative tumor-specific T cells with signatures of exhaustion and antigen experience, including high expression of immune checkpoint molecules, were

locally restricted, which is in contrast with a systemic antitumor immunity, recently described in breast cancer (*37*). This may explain why checkpoint inhibition is a promising therapeutic strategy in several solid tumors (*46*, *47*) but has shown rather disappointing results in MM (*48*, *49*). Yet, functional imaging is required to monitor localized therapy responses (*50*), which are possible given the strong differences in tumor immunology between breakout lesions and diffusely infiltrated BM. Furthermore, although less favorable outcomes after T cell redirecting therapies, including bispecific antibodies and CAR-T cell therapies, are mainly associated with EMD (*51–54*), our results suggest that the distinct genomic and TME features of paramedullary disease (i.e., breakout lesions) need to be considered when linking EMD biology to clinical outcomes in future studies to unravel the mechanisms underlying poor survival. Together, our study highlights the importance of studying the coevolution of myeloma and its TME within and outside the BM. We uncover breakout lesions as major sites for tumor evolution and immune cell diversification, representing a key event in myeloma pathogenesis and tumor immunity with potential therapeutic implications.

MATERIALS AND METHODS
Study design
This study aimed to elucidate the early processes associated with BM independence in MM by characterizing the cellular composition and tumor-immune interactions in breakout lesions compared with rBM samples. Using a 23-plex cytometry panel, we systematically mapped all major BM-resident cell types in breakout and intramedullary lesions, alongside comparison samples, including paired rBM stamps, liquid aspirates from rBM sites, and PB. This analysis was complemented by a 23-plex T cell panel to provide a detailed characterization of the T cell landscape. To further investigate cellular and immunological states, CITE-seq combined with single-cell TCR-seq was performed on flow cytometry–enriched plasma cells, myeloid cells, NK cells, T cells, stromal cells, and endothelial cells from breakout lesions and matched rBM samples. To explore intralesion heterogeneity and examine the relationship between genomic diversification and clonal T cell expansions, breakout lesions were subdivided into spatially defined microregions for cytometric ecotyping, single-cell and bulk TCR-seq, and WGS. IHC for CD8, CD68, and MUM1 and highly multiplexed immunofluorescence imaging were performed to investigate the unbalanced distribution of immune cells in different subregions of breakout lesions.

Patients
We included 54 samples from 16 patients with NDMM fulfilling the IMWG (International Myeloma Working Group) criteria for treatment (fig. S1, A and B) (*4*). For validation purposes, we used trephine biopsies and/or WGS data from 21 additional patients, including 19 patients from a recently published study (*11*) (fig. S1B). Patients' characteristics, follow-up data, the origin of samples, and the analyses, which were performed with the samples, are shown in data files S1 and S2 and fig. S1B. Informed consent for sample collection and processing in accordance with the Declaration of Helsinki was obtained for all cases included in this study that had been approved by the Heidelberg University Medical Faculty ethics review board (S278-13).

Medical imaging
Osteolytic lesions were diagnosed using whole-body computer tomography (CT). CT-guided sampling of focal lesions was performed using a Siemens Emotion 16 CT (Siemens Co., Erlangen, Germany) as recently described (*11*). Surgical resections were performed in patients with clinical indication for stabilization of the spine.

Sample preparation
The Ficoll-Paque method was used to isolate mononuclear cells from BM aspirates and PB. CD138$^+$ MM cells from aspirates were enriched by immunomagnetic selection (Robosep, STEMCELL Technologies). CD138$^+$ and CD138$^-$ cells were either preserved in Qiagen RLT buffer for bulk sequencing at −80°C or viably frozen in 10% dimethyl sulfoxide for single-cell sequencing and flow cytometry at −150°C. Dry cell pellets were stored at −20°C. Enzymatic digestion of samples from surgical resections and BM stamps was performed following a previously described method (*11*). For seven patients, specimens obtained from surgical resections were divided into microregions before enzymatic digestion (data file S2). To enrich MM cells from digested samples, cells were sorted (CD38-high, HLA-DR–negative, CD3-negative, and CD45-positive) using a FACSAria (BD Biosciences). Dead cells were identified using eFluor-506 (Thermo Fisher Scientific, USA). Sorted cells were stored in RLT buffer (Qiagen, Hilden, Germany) at −80°C. The same gating strategy as that for CITE-seq was used (fig. S5A). Sample availability and processing methods are shown in data file S2.

Flow cytometry
Rainbow Calibration Particles (BD Biosciences) were used for voltage adjustment. Compensation controls were prepared using UltraComp eBeads Compensation Beads (Thermo Fisher Scientific). Efluor compensation controls were prepared using BMMCs (BM mononuclear cells) or PBMCs. Antibody master mixes were prepared in Brilliant Stain Buffer Plus (BD Biosciences). Antibody panels are shown in tables S1, S2, and S4. Cryopreserved samples were thawed at 37°C, resuspended in RPMI with 10% fetal calf serum (FCS), and centrifuged at 500*g* for 5 min, and the pellet was resuspended in a 400-μl fluorescence-activated cell sorting (FACS) buffer [1× Dulbecco's phosphate-buffered saline (DPBS), 5% FCS, and 0.5 mM EDTA]. All following steps were performed in a Nunc 96-Well Polystyrene Conical Bottom MicroWell Plate. First, cells were centrifuged at 500*g* for 5 min, and the pellet was resuspended in a total volume of 30 μl with eFluor-506 fixable viability dye (eBioscience, 1:1000 dilution) and FcR Blocking Reagent (Miltenyi Biotec, 1:20 dilution). After 5 min at room temperature (RT) in the dark, 50 μl of antibody master mix was added. After 15 min at 4°C in the dark, 120 μl of FACS buffer was added, the plate was centrifuged at 500*g* for 5 min, and the pellet was resuspended in 200 μl of FACS buffer. A third washing step with 200 μl of FACS buffer was performed, before cells were resuspended in 30 μl of FACS buffer and transferred to a 1.2-ml individual reaction tube (Starlab) for flow cytometry using a BD FACSymphony A5 Cell Analyzer. A reference control sample was measured for each plate. See Supplementary Materials and Methods for a detailed description of the analysis of flow cytometry data.

Single-cell RNA sequencing including CITE-seq and V(D)J sequencing
Cryopreserved samples were thawed at 37°C, resuspended in 10 ml of RPMI with 10% FCS, and centrifuged at 300*g* for 5 min. The pellet

was resuspended in 10 ml of RPMI with 10% FCS. Cells were centrifuged at 300g for 5 min, and the pellet was resuspended in 50 to 100 µl of phosphate-buffered saline (PBS) plus calcein (0.1 µM 1:100 from 10 µM diluted stock) and eFluor-506 fixable viability dye (eBioscience, 1:1000). After 5 min at RT, 100 to 200 µl of antibody master mix for FACS sorting (table S3) was added. Individual samples were hashed by adding 0.1 µg of TotalSeq of the respective anti-human Hashtag 1 to 4 or 6 to 9 (BioLegend). After 15 min at 4°C, 5 ml of FACS buffer (1x DPBS, 5% FCS, and 0.5 mM EDTA) was added, the tube was centrifuged at 300g for 5 min, and the pellet was resuspended in 300 µl of FACS buffer. Sorting was performed with a BD FACSAria. Gating strategy is shown in fig. S5A. For each cell population and sample, a maximum of 10,000 events (range = 3500 to 10,000 per population, CD90+CD34+ all cells) were sorted into 1.5-ml protein low binding Eppendorf tubes prefilled with 150 µl of cell staining buffer (BioLegend). Sorted cells were pooled into batches, where paired samples from the same patient were in different batches. Each batch contained ~130,000 sorted cells, which were centrifuged at 300g for 5 min, and the pellet was resuspended in 25 µl of cell staining buffer. Subsequently, 2.5 µl of Human TruStain FcX Blocking reagent (BioLegend) was added to the pooled cell suspension and incubated for 10 min at 4°C. After adding 25 µl of reconstituted TotalSeq-C antibody cocktail (BioLegend), cells were incubated for 30 min at 4°C. Cells were washed three times with 3.5 ml of cell staining buffer and resuspended in PBS and loaded onto three 10x gel beads in emulsion (GEMs) (22,000 to 24,000 cells per GEM) per batch. Immunoprofiling was performed according to the Chromium Next GEM Single Cell 5′ Reagent Kit v2 (Dual Index) user guide with feature barcode technology for cell surface protein and immune receptor mapping (10x Genomics; CG000330 Rev A). Generated gene expression (GEX) and protein (ADT) libraries were paired-end sequenced on the NovaSeq 6000 S4 (~100,000 mean reads per cell). Generated V(D)J libraries were paired-end sequenced on the NextSeq 550 (~18,000 mean reads per cell). A detailed description of the analysis of the CITE-seq data is provided in Supplementary Materials and Methods.

Whole-genome sequencing

DNA was extracted using the Allprep Kit (Qiagen). The Illumina TruSeq Nano DNA kit was used to generate WGS libraries, which were sequenced on a NovaSeq 6000 S4 flow cell (paired-end 150 base pairs) with an average coverage of 85x for tumor and 43x for germline samples. Using the DKFZ OTP WGS pipeline (55), the raw sequencing data were processed and aligned to the human reference genome build 37 version hs37d5 (55). Copy number aberrations were identified with ACEseq (v1.2.8-4) (56), single-nucleotide variants (SNVs) were called with samtools mpileup (v1.2.166-3) (57), and indels were detected with platyphus (v2.4.1-1) (58). Additional filtering steps for SNVs included blacklist filtering (58), fpfilter (https://github.com/genome/fpfilter-tool), and exclusion of SNVs located in immunoglobulin regions. For SNVs detected in only one of the paired samples, Rsamtools (v2.6.0) was used to quantify variant reads in both samples. Manual refinement of somatic variants was conducted using IGV (v2.7.2) (59), following published best-practice guidelines (60).

Deep/bulk TCR-seq

DNA was isolated using the Allprep Kit (Qiagen), and CDR3β sequencing was performed by immunoSEQ (Adaptive Biotechnology, Seattle, WA). Data were analyzed using the immunoSEQ ANALYZER 3.0 (Adaptive Biotechnology, Seattle WA), with only productive CDR3β rearrangements used for TCR frequency calculations. TCR clones representing ≥1% of the total T cell population and showing a fold change of ≥10 between the breakout lesion and rBM stamp or between regions within the same lesion were considered enriched.

Immunohistochemistry

Tissue blocks containing MUM1-positive myeloma cells were selected for analysis. Sections were cut at 2 µm in thickness using a standard microtome, and slides were dried overnight at RT. Immunohistochemical staining was performed on consecutive tissue sections using the Ventana Benchmark Ultra automated immunostainer (Roche, USA). Proteins stained included MUM1 (mouse anti-human, clone Mum1p, Agilent DAKO, Santa Clara, USA), CD68 (mouse anti-human, clone KP-1, Roche Ventana, USA), and CD8 (rabbit anti-human, clone SP57, Roche Ventana, USA). For eight patients, CD68 (DAB) and CD8 (FastRed) were costained on the same section. Images of stained slides were captured at RT using the Aperio AT2 slide scanner at ×40 magnification (Leica 20x/0.75NA Plan Apo objective with 2x automatic optical magnification changer; resolution: 0.25 µm/pixel) and the manufacturer's acquisition software suite (Leica Biosystems, Nussloch, Germany, version 102.0.7.5). Focus points were automatically set using the software's focusing strategy and manually corrected if placed in areas without tissue. The images were analyzed with the QuPath software (v0.3.2), importing them via the Bioformats builder. An expert pathologist performed a final review of all stained slides and detected cells.

Multiplex imaging

Formalin-fixed paraffin-embedded (FFPE) tissue sections (2 µm) were incubated at 60°C for 30 min and deparaffinized in Histo-Clear II for 20 min before being rehydrated in a graded alcohol series (ethanol:deionized water, 100:0, 100:0, 90:10, 70:30, 50:50, and 70:30; 3 min each). The slides were washed twice in 20 mM Tris and 150 mM NaCl (pH 7.6) [tris-buffered saline (TBS)] for 5 min, and antigen retrieval was performed in tris-EDTA buffer (pH 9) with 0.05% Tween 20 for 20 min at 100°C. After cooling to RT, the slides were washed twice in TBS for 5 min. Autofluorescence was quenched by submersing the slides in PBS with 2% H_2O_2 and 20 mM NaOH for 30 min at RT and concomitant light exposure using a 10,000-lux light-emitting diode (LED) lamp (RHM). After two washes in TBS for 5 min, the tissue was blocked with 3% bovine serum albumin (BSA) and 2.5% goat serum in TBS for 30 min at RT. The samples were stained with anti-MUM1 (clone Mum1p, mouse) at 1:50 and anti–forkhead box protein P3 (FOXP3) (clone SP97, rabbit) at 1:50 in 1% BSA in TBS overnight at 4°C and washed twice with TBS for 5 min. Multiplex immunofluorescence was performed using the antibody panel described in table S5 and the Lunaphore COMET platform (Biotechne). For the validation experiment, paired box 5 (PAX5) was replaced with CD20, and CD7 was added to the panel (table S5). The COMET platform is equipped with an LED-based wide-field microscope and 20× objective that acquires images in three fluorescent channels [DAPI (4′,6-diamidino-2-phenylindole), TRITC (tetramethyl rhodamine isothiocyanate), and Cy5], providing subcellular resolution and an image pixel size of 0.23 µm (61). A detailed description of the analysis of the imaging data is provided in Supplementary Materials and Methods.

Statistical analysis

Statistical analyses were carried out using the R software package v4.3.3 and v4.4.0. Group comparisons of continuous variables were done using the two-sided Wilcoxon rank sum test for unpaired samples and the two-sided Wilcoxon signed-rank test for paired samples. P values were corrected for multiple comparisons using the Benjamini-Hochberg method. Correlation coefficients were determined using Pearson correlation or linear mixed-effects models. Similarity between correlation matrices was assessed using the Mantel test. Differential abundant cell type frequencies were calculated as a $\log_2$(fold change), adding one cell to each cell type per sample before the comparisons to avoid cell frequencies of 0.

Supplementary Materials

The PDF file includes:

Materials and Methods
Figs. S1 to S12
Tables S1 to S5
References (*62–79*)

Other Supplementary Material for this manuscript includes the following:

Data files S1 to S7
MDAR Reproducibility Checklist

REFERENCES AND NOTES

1. A. McCurdy, H. Seow, G. P. Pond, A. Gayowsky, R. Chakraborty, A. Visram, R. Kaedbey, A. D'Souza, G. R. Mohyuddin, T. M. Wildes, R. Fonseca, H. Mian, Cancer-specific mortality in multiple myeloma: A population-based retrospective cohort study. *Haematologica* **108**, 3384–3391 (2023).

2. A. J. Cowan, D. J. Green, M. Kwok, S. Lee, D. G. Coffey, L. A. Holmberg, S. Tuazon, A. K. Gopal, E. N. Libby, Diagnosis and management of multiple myeloma: A review. *JAMA* **327**, 464–477 (2022).

3. J. Hillengass, K. Fechtner, M.-A. Weber, T. Bäuerle, S. Ayyaz, C. Heiss, T. Hielscher, T. M. Moehler, G. Egerer, K. Neben, A. D. Ho, H.-U. Kauczor, S. Delorme, H. Goldschmidt, Prognostic significance of focal lesions in whole-body magnetic resonance imaging in patients with asymptomatic multiple myeloma. *J. Clin. Oncol.* **28**, 1606–1610 (2010).

4. S. V. Rajkumar, M. A. Dimopoulos, A. Palumbo, J. Blade, G. Merlini, M.-V. Mateos, S. Kumar, J. Hillengass, E. Kastritis, P. Richardson, O. Landgren, B. Paiva, A. Dispenzieri, B. Weiss, X. LeLeu, S. Zweegman, S. Lonial, L. Rosinol, E. Zamagni, S. Jagannath, O. Sezer, S. Y. Kristinsson, J. Caers, S. Z. Usmani, J. J. Lahuerta, H. E. Johnsen, M. Beksac, M. Cavo, H. Goldschmidt, E. Terpos, R. A. Kyle, K. C. Anderson, B. G. M. Durie, J. F. S. Miguel, International Myeloma Working Group updated criteria for the diagnosis of multiple myeloma. *Lancet Oncol.* **15**, e538–e548 (2014).

5. R. Walker, B. Barlogie, J. Haessler, G. Tricot, E. Anaissie, J. D. Shaughnessy Jr., J. Epstein, R. van Hemert, E. Erdem, A. Hoering, J. Crowley, E. Ferris, K. Hollmig, F. van Rhee, M. Zangari, M. Pineda-Roman, A. Mohiuddin, S. Yaccoby, J. Sawyer, E. J. Angtuaco, Magnetic resonance imaging in multiple myeloma: Diagnostic and clinical implications. *J. Clin. Oncol.* **25**, 1121–1128 (2007).

6. L. Rasche, S. S. Chavan, O. W. Stephens, P. H. Patel, R. Tytarenko, C. Ashby, M. Bauer, C. Stein, S. Deshpande, C. Wardell, T. Buzder, G. Molnar, M. Zangari, F. van Rhee, S. Thanendrarajan, C. Schinke, J. Epstein, F. E. Davies, B. A. Walker, T. Meissner, B. Barlogie, G. J. Morgan, N. Weinhold, Spatial genomic heterogeneity in multiple myeloma revealed by multi-region sequencing. *Nat. Commun.* **8**, 268 (2017).

7. J. Bladé, M. Beksac, J. Caers, A. Jurczyszyn, M. von Lilienfeld-Toal, P. Moreau, L. Rasche, L. Rosiñol, S. Z. Usmani, E. Zamagni, P. Richardson, Extramedullary disease in multiple myeloma: A systematic literature review. *Blood Cancer J.* **12**, 45 (2022).

8. N. Gagelmann, D. Dima, M. Merz, H. Hashmi, N. Ahmed, N. Tovar, A. Oliver-Caldés, F. Stölzel, K. Rathje, L. Fischer, P. Born, L. Schäfer, A.-M. Albici, N. Schub, S. Kfir-Erenfeld, M. Assayag, N. Asherie, G. G. Wulf, S. Kharboutli, F. Müller, L. Shune, J. A. Davis, F. Anwer, V. Vucinic, U. Platzbecker, F. Ayuk, N. Kröger, J. Khouri, C. Gurnari, J. McGuirk, P. Stepensky, A.-O. Abdallah, C. Fernández de Larrea, Development and validation of a prediction model of outcome after B-cell maturation antigen-directed chimeric antigen receptor T-cell therapy in relapsed/refractory multiple myeloma. *J. Clin. Oncol.* **42**, 1665–1675 (2024).

9. N. Korde, S. Y. Kristinsson, O. Landgren, Monoclonal gammopathy of undetermined significance (MGUS) and smoldering multiple myeloma (SMM): Novel biological insights and development of early treatment strategies. *Blood* **117**, 5573–5581 (2011).

10. S. Forster, R. Radpour, Molecular impact of the tumor microenvironment on multiple myeloma dissemination and extramedullary disease. *Front. Oncol.* **12**, 941437 (2022).

11. L. John, A. M. Poos, A. Brobeil, C. Schinke, S. Huhn, N. Prokoph, R. Lutz, B. Wagner, M. Zangari, S. M. Tirier, J.-P. Mallm, S. Schumacher, D. Vonficht, L. Solé-Boldo, S. Quick, S. Steiger, M. J. Przybilla, K. Bauer, A. Baumann, S. Hemmer, C. Rehnitz, C. Lückerath, C. Sachpekidis, G. Mechtersheimer, U. Haberkorn, A. Dimitrakopoulou-Strauss, P. Reichert, B. Barlogie, C. Müller-Tidow, H. Goldschmidt, J. Hillengass, L. Rasche, S. F. Haas, F. van Rhee, K. Rippe, M. S. Raab, S. Sauer, N. Weinhold, Resolving the spatial architecture of myeloma and its microenvironment at the single-cell level. *Nat. Commun.* **14**, 5011 (2023).

12. M. M. E. de Jong, L. Chen, M. H. G. P. Raaijmakers, T. Cupedo, Bone marrow inflammation in haematological malignancies. *Nat. Rev. Immunol.* **24**, 543–558 (2024).

13. E. Zhao, H. Xu, L. Wang, I. Kryczek, K. Wu, Y. Hu, G. Wang, W. Zou, Bone marrow and the control of immunity. *Cell. Mol. Immunol.* **9**, 11–19 (2012).

14. L. Rasche, E. J. Angtuaco, T. L. Alpe, G. H. Gershner, J. E. McDonald, R. S. Samant, M. Kumar, R. Van Hemert, J. Epstein, S. Deshpande, R. Tytarenko, S. Yaccoby, J. Hillengass, S. Thanendrarajan, C. Schinke, F. van Rhee, M. Zangari, B. A. Walker, B. Barlogie, G. J. Morgan, F. E. Davies, N. Weinhold, The presence of large focal lesions is a strong independent prognostic factor in multiple myeloma. *Blood* **132**, 59–66 (2018).

15. S. Triana, D. Vonficht, L. Jopp-Saile, S. Raffel, R. Lutz, D. Leonce, M. Antes, P. Hernández-Malmierca, D. Ordoñez-Rueda, B. Ramasz, T. Boch, J.-C. Jann, D. Nowak, W.-K. Hofmann, C. Müller-Tidow, D. Hübschmann, T. Alexandrov, V. Benes, A. Trumpp, M. Paulsen, L. Velten, S. Haas, Single-cell proteo-genomic reference maps of the hematopoietic system enable the purification and massive profiling of precisely defined cell states. *Nat. Immunol.* **22**, 1577–1589 (2021).

16. C. Baccin, J. Al-Sabah, L. Velten, P. M. Helbling, F. Grünschläger, P. Hernández-Malmierca, C. Nombela-Arrieta, L. M. Steinmetz, A. Trumpp, S. Haas, Combined single-cell and spatial transcriptomics reveal the molecular, cellular and spatial bone marrow niche organization. *Nat. Cell Biol.* **22**, 38–48 (2020).

17. M. M. E. de Jong, Z. Kellermayer, N. Papazian, S. Tahri, D. Hofste Op Bruinink, R. Hoogenboezem, M. A. Sanders, P. C. van de Woestijne, P. K. Bos, C. Khandanpour, J. Vermeulen, P. Moreau, M. van Duin, A. Broijl, P. Sonneveld, T. Cupedo, The multiple myeloma microenvironment is defined by an inflammatory stromal cell landscape. *Nat. Immunol.* **22**, 769–780 (2021).

18. J. C. Schupp, T. S. Adams, C. Cosme Jr., M. S. B. Raredon, Y. Yuan, N. Omote, S. Poli, M. Chioccioli, K.-A. Rose, E. P. Manning, M. Sauler, G. Deluliis, F. Ahangari, N. Neumark, A. C. Habermann, A. J. Gutierrez, L. T. Bui, R. Lafyatis, R. W. Pierce, K. B. Meyer, M. C. Nawijn, S. A. Teichmann, N. E. Banovich, J. A. Kropski, L. E. Niklason, D. Pe'er, X. Yan, R. J. Homer, I. O. Rosas, N. Kaminski, Integrated single-cell atlas of endothelial cells of the human lung. *Circulation* **144**, 286–302 (2021).

19. L.-F. He, T.-T. Wang, Q.-Y. Gao, G.-F. Zhao, Y.-H. Huang, L.-K. Yu, Y.-Y. Hou, Stanniocalcin-1 promotes tumor angiogenesis through up-regulation of VEGF in gastric cancer cells. *J. Biomed. Sci.* **18**, 1–9 (2011).

20. M. Liu, L. Zhang, G. Marsboom, A. Jambusaria, S. Xiong, P. T. Toth, E. V. Benevolenskaya, J. Rehman, A. B. Malik, Sox17 is required for endothelial regeneration following inflammation-induced vascular injury. *Nat. Commun.* **10**, 1–14 (2019).

21. A. M. N. Walker, N. Warmke, B. Mercer, N. T. Watt, R. Mughal, J. Smith, S. Galloway, N. J. Haywood, T. Soomro, K. J. Griffin, S. B. Wheatcroft, N. Y. Yuldasheva, D. J. Beech, P. Carmeliet, M. T. Kearney, R. M. Cubbon, Endothelial insulin receptors promote VEGF-A signaling via ERK1/2 and sprouting angiogenesis. *Endocrinology* **162**, bqab104 (2021).

22. N. M. Moll, R. M. Ransohoff, CXCL12 and CXCR4 in bone marrow physiology. *Expert Rev. Hematol.* **3**, 315–322 (2010).

23. M. Foroutan, R. Molania, A. Pfefferle, C. Behrenbruch, S. Scheer, A. Kallies, T. P. Speed, J. Cursons, N. D. Huntington, The ratio of exhausted to resident infiltrating lymphocytes is prognostic for colorectal cancer patient outcome. *Cancer Immunol. Res.* **9**, 1125–1140 (2021).

24. L. F. de Andrade, Y. Lu, A. Luoma, Y. Ito, D. Pan, J. W. Pyrdol, C. H. Yoon, G.-C. Yuan, K. W. Wucherpfennig, Discovery of specialized NK cell populations infiltrating human melanoma metastases. *JCI Insight* **4**, e133103 (2019).

25. E. Azizi, A. J. Carr, G. Plitas, A. E. Cornish, C. Konopacki, S. Prabhakaran, J. Nainys, K. Wu, V. Kiseliovas, M. Setty, K. Choi, R. M. Fromme, P. Dao, P. T. McKenney, R. C. Wasti, K. Kadaveru, L. Mazutis, A. Y. Rudensky, D. Pe'er, Single-cell map of diverse immune phenotypes in the breast tumor microenvironment. *Cell* **174**, 1293–1308.e36 (2018).

26. G. Oliveira, K. Stromhaug, S. Klaeger, T. Kula, D. T. Frederick, P. M. Le, J. Forman, T. Huang, S. Li, W. Zhang, Q. Xu, N. Cieri, K. R. Clauser, S. A. Shukla, D. Neuberg, S. Justesen, G. MacBeath, S. A. Carr, E. F. Fritsch, N. Hacohen, M. Sade-Feldman, K. J. Livak, G. M. Boland, P. A. Ott, D. B. Keskin, C. J. Wu, Phenotype, specificity and avidity of antitumour CD8 T cells in melanoma. *Nature* **596**, 119–125 (2021).

27. F. J. Lowery, S. Krishna, R. Yossef, N. B. Parikh, P. D. Chatani, N. Zacharakis, M. R. Parkhurst, N. Levin, S. Sindiri, A. Sachs, K. J. Hitscherich, Z. Yu, N. R. Vale, Y.-C. Lu, Z. Zheng, L. Jia, J. J. Gartner, V. K. Hill, A. R. Copeland, S. K. Nah, R. V. Masi, B. Gasmi, S. Kivitz, B. C. Paria, M. Florentin, S. P. Kim, K.-I. Hanada, Y. F. Li, L. T. Ngo, S. Ray, M. L. Shindorf, S. T. Levi,

R. Shepherd, C. Toy, A. Y. Parikh, T. D. Prickett, M. C. Kelly, R. Beyer, S. L. Goff, J. C. Yang, P. F. Robbins, S. A. Rosenberg, Molecular signatures of antitumor neoantigen-reactive T cells from metastatic human cancers. *Science* **375**, 877–884 (2022).

28. R. Yang, S. Cheng, N. Luo, R. Gao, K. Yu, B. Kang, L. Wang, Q. Zhang, Q. Fang, L. Zhang, C. Li, A. He, X. Hu, J. Peng, X. Ren, Z. Zhang, Distinct epigenetic features of tumor-reactive CD8^{+} T cells in colorectal cancer patients revealed by genome-wide DNA methylation analysis. *Genome Biol.* **21**, 2 (2019).

29. G. Caravagna, T. Heide, M. J. Williams, L. Zapata, D. Nichol, K. Chkhaidze, W. Cross, G. D. Cresswell, B. Werner, A. Acar, L. Chesler, C. P. Barnes, G. Sanguinetti, T. A. Graham, A. Sottoriva, Subclonal reconstruction of tumors by using machine learning and population genetics. *Nat. Genet.* **52**, 898–907 (2020).

30. C. M. Schürch, S. S. Bhate, G. L. Barlow, D. J. Phillips, L. Noti, I. Zlobec, P. Chu, S. Black, J. Demeter, D. R. McIlwain, S. Kinoshita, N. Samusik, Y. Goltsev, G. P. Nolan, Coordinated cellular neighborhoods orchestrate antitumoral immunity at the colorectal cancer invasive front. *Cell* **183**, 838 (2020).

31. C. Schinke, A. M. Poos, M. Bauer, L. John, S. Johnson, S. Deshpande, L. Carrillo, D. Alapat, L. Rasche, S. Thanendrarajan, M. Zangari, S. Al Hadidi, F. van Rhee, F. Davies, M. S. Raab, G. Morgan, N. Weinhold, Characterizing the role of the immune microenvironment in multiple myeloma progression at a single-cell level. *Blood Adv.* **6**, 5873–5883 (2022).

32. L. Rasche, C. Schinke, F. Maura, M. A. Bauer, C. Ashby, S. Deshpande, A. M. Poos, M. Zangari, S. Thanendrarajan, F. E. Davies, B. A. Walker, B. Barlogie, O. Landgren, G. J. Morgan, F. van Rhee, N. Weinhold, The spatio-temporal evolution of multiple myeloma from baseline to relapse-refractory states. *Nat. Commun.* **13**, 4517 (2022).

33. I. Yofe, T. Shami, N. Cohen, T. Landsberger, F. Sheban, L. Stoler-Barak, A. Yalin, T. S. Phan, B. Li, N. Monteran, Y. 'ela Scharff, A. Giladi, A. Elbaz, E. David, A. Gurevich-Shapiro, C. Gur, Z. Shulman, N. Erez, I. Amit, Spatial and temporal mapping of breast cancer lung metastases identify TREM2 macrophages as regulators of the metastatic boundary. *Cancer Discov.* **13**, 2610–2631 (2023).

34. R. N. Ramos, Y. Missolo-Koussou, Y. Gerber-Ferder, C. P. Bromley, M. Bugatti, N. G. Núñez, J. T. Boari, W. Richer, L. Menger, J. Denizeau, C. Sedlik, P. Caudana, F. Kotsias, L. L. Niborski, S. Viel, M. Bohec, S. Lameiras, S. Baulande, L. Lesage, A. Nicolas, D. Meseure, A. Vincent-Salmon, F. Reyal, C.-A. Dutertre, F. Ginhoux, L. Vimeux, E. Donnadieu, B. Buttard, J. Galon, S. Zelenay, W. Vermi, P. Guermonprez, E. Piaggio, J. Helft, Tissue-resident FOLR2^{+} macrophages associate with CD8^{+} T cell infiltration in human breast cancer. *Cell* **185**, 1189–1207.e25 (2022).

35. M. Molgora, Y. A. Liu, M. Colonna, M. Cella, TREM2: A new player in the tumor microenvironment. *Semin. Immunol.* **67**, 101739 (2023).

36. N. V. Gavil, M. C. Scott, E. Weyu, O. C. Smith, S. D. O'Flanagan, S. Wijeyesinghe, S. Lotfi-Emran, S. L. Shiao, V. Vezys, D. Masopust, Chronic antigen in solid tumors drives a distinct program of T cell residence. *Sci. Immunol.* **8**, eaad5976 (2023).

37. Y. J. Lee, Y. J. Kim, S. H. Jeon, H. Nam, H. H. Jung, M. Jeon, E.-S. Kim, S. J. Bae, J. Ahn, T.-K. Yoo, W. Y. Sun, S. G. Ahn, J. Jeong, S.-H. Park, W. C. Park, S. I. Kim, E.-C. Shin, CD39^{+} tissue-resident memory CD8^{+} T cells with a clonal overlap across compartments mediate antitumor immunity in breast cancer. *Sci. Immunol.* **7**, eabn8390 (2022).

38. J. K. Bailur, S. S. McCachren, D. B. Doxie, M. Shrestha, K. Pendleton, A. K. Nooka, N. Neparidze, T. L. Parker, N. Bar, J. L. Kaufman, C. C. Hofmeister, L. H. Boise, S. Lonial, M. L. Kemp, K. M. Dhodapkar, M. V. Dhodapkar, Early alterations in stem-like/resident T cells, innate and myeloid cells in the bone marrow in preoplastic gammopathy. *JCI Insight* **5**, 31013254 (2019).

39. O. Zavidij, N. J. Haradhvala, T. H. Mouhieddine, R. Sklavenitis-Pistofidis, S. Cai, M. Reidy, M. Rahmat, A. Flaifel, B. Ferland, N. K. Su, M. P. Agius, J. Park, S. Manier, M. Bustoros, D. Huynh, B. Berrios, C.-J. Liu, M. X. He, E. Braggio, R. Fonseca, Y. E. Maruvka, J. L. Guerriero, M. Goldman, E. M. Van Allen, S. A. McCarroll, J. Azzi, G. Getz, I. M. Ghobrial, Single-cell RNA sequencing reveals compromised immune microenvironment in precursor stages of multiple myeloma. *Nat. Cancer* **1**, 493–506 (2020).

40. W. Pilcher, B. E. Thomas, S. S. Bhasin, R. G. Jayasinghe, L. Yao, E. Gonzalez-Kozlova, S. Dasari, S. Kim-Schulze, A. Rahman, J. Patton, M. Fiala, G. Cheloni, T. Kourelis, M. V. Dhodapkar, R. Vij, S. Mehr, M. Hamilton, H. J. Cho, D. Auclair, D. E. Avigan, S. K. Kumar, S. Gnjatic, L. Ding, M. Bhasin, Cross center single-cell RNA sequencing study of the immune microenvironment in rapid progressing multiple myeloma. *NPJ Genom. Med.* **8**, 3 (2023).

41. K. M. Dhodapkar, A. D. Cohen, A. Kaushal, A. L. Garfall, R. J. Manalo, A. R. Carr, S. S. McCachren, E. A. Stadtmauer, S. F. Lacey, J. J. Melenhorst, C. H. June, M. C. Milone, M. V. Dhodapkar, Changes in bone marrow tumor and immune cells correlate with durability of remissions following BCMA CAR T therapy in myeloma. *Blood Cancer Discov.* **3**, 490–501 (2022).

42. M. J. Friedrich, P. Neri, N. Kehl, J. Michel, S. Steiger, M. Kilian, N. Leblay, R. Maity, R. Sankowski, H. Lee, E. Barakat, S. Ahn, N. Weinhold, K. Rippe, L. Bunse, M. Platten, H. Goldschmidt, C. Müller-Tidow, M.-S. Raab, N. J. Bahlis, The pre-existing T cell landscape determines the response to bispecific T cell engagers in multiple myeloma patients. *Cancer Cell* **41**, 711–725.e6 (2023).

43. C. Sautès-Fridman, F. Petitprez, J. Calderaro, W. H. Fridman, Tertiary lymphoid structures in the era of cancer immunotherapy. *Nat. Rev. Cancer* **19**, 307–325 (2019).

44. M. H. Robinson, N. Y. Villa, D. L. Jaye, A. K. Nooka, A. Duffy, S. S. McCachren, J. Manalo, J. M. Switchenko, S. Barnes, S. Potdar, M. I. Azeem, A. A. Horvat, V. C. Parihar, J. Gong, Y. Liang, G. H. Smith, V. A. Gupta, L. H. Boise, J. L. Kaufman, C. C. Hofmeister, N. S. Joseph, S. Lonial, K. M. Dhodapkar, M. V. Dhodapkar, Regulation of antigen-specific T cell infiltration and spatial architecture in multiple myeloma and premalignancy. *J. Clin. Invest.* **133**, e167629 (2023).

45. O. Barboy, A. Bercovich, H. Li, Y. Eyal-Lubling, A. Yalin, Y. S. Itai, K. Abadie, M. Zada, E. David, S. Shlomi-Loubaton, Y. Katzenelenbogen, D. A. Jaitin, C. Gur, I. Yofe, T. Feferman, M. Cohen, R. Dahan, E. W. Newell, A. Lifshitz, A. Tanay, I. Amit, Modeling T cell temporal response to cancer immunotherapy rationalizes development of combinatorial treatment protocols. *Nat. Cancer* **5**, 18 (2024).

46. Q. Sun, Z. Hong, C. Zhang, L. Wang, Z. Han, D. Ma, Immune checkpoint therapy for solid tumours: Clinical dilemmas and future trends. *Signal Transduct. Target. Ther.* **8**, 320 (2023).

47. C. Robert, A decade of immune-checkpoint inhibitors in cancer therapy. *Nat. Commun.* **11**, 3801 (2020).

48. M.-V. Mateos, H. Blacklock, F. Schjesvold, A. Oriol, D. Simpson, A. George, H. Goldschmidt, A. Larocca, A. Chanan-Khan, D. Sherbenou, I. Avivi, N. Benyamini, S. Iida, M. Matsumoto, K. Suzuki, V. Ribrag, S. Z. Usmani, S. Jagannath, E. M. Ocio, P. Rodriguez-Otero, J. San Miguel, U. Kher, M. Farooqui, J. Liao, P. Marinello, S. Lonial, KEYNOTE-183 Investigators, Pembrolizumab plus pomalidomide and dexamethasone for patients with relapsed or refractory multiple myeloma (KEYNOTE-183): A randomised, open-label, phase 3 trial. *Lancet Haematol.* **6**, e459–e469 (2019).

49. Z. Liu, X. Xu, H. Liu, X. Zhao, C. Yang, R. Fu, Immune checkpoint inhibitors for multiple myeloma immunotherapy. *Exp. Hematol. Oncol.* **12**, 99 (2023).

50. L. Rasche, D. Alapat, M. Kumar, G. Gershner, J. McDonald, C. P. Wardell, R. Samant, R. Van Hemert, J. Epstein, A. F. Williams, S. Thanendrarajan, C. Schinke, M. Bauer, C. Ashby, R. G. Tytarenko, F. van Rhee, B. A. Walker, M. Zangari, B. Barlogie, F. E. Davies, G. J. Morgan, N. Weinhold, Combination of flow cytometry and functional imaging for monitoring of residual disease in myeloma. *Leukemia* **33**, 1713–1722 (2019).

51. N. C. Munshi, L. D. Anderson Jr., N. Shah, D. Madduri, J. Berdeja, S. Lonial, N. Raje, Y. Lin, D. Siegel, A. Oriol, P. Moreau, I. Yakoub-Agha, M. Delforge, M. Cavo, H. Einsele, H. Goldschmidt, K. Weisel, A. Rambaldi, D. Reece, F. Petrocca, M. Massaro, J. N. Connarn, S. Kaiser, P. Patel, L. Huang, T. B. Campbell, K. Hege, J. San-Miguel, Idecabtagene vicleucel in relapsed and refractory multiple myeloma. *N. Engl. J. Med.* **384**, 705–716 (2021).

52. J. San-Miguel, B. Dhakal, K. Yong, A. Spencer, S. Anguille, M.-V. Mateos, C. Fernández de Larrea, J. Martínez-López, P. Moreau, C. Touzeau, X. Leleu, I. Avivi, M. Cavo, T. Ishida, S. J. Kim, W. Roeloffzen, N. W. C. J. van de Donk, D. Dytfeld, S. Sidana, L. J. Costa, A. Oriol, R. Popat, A. M. Khan, Y. C. Cohen, P. J. Ho, J. Griffin, N. Lendvai, C. Lonardi, A. Slaughter, J. M. Schecter, C. C. Jackson, K. Connors, K. Li, E. Zudaire, D. Chen, J. Gilbert, T.-M. Yeh, S. Nagle, E. Florendo, L. Pacaud, N. Patel, S. J. Harrison, H. Einsele, Cilta-cel or standard care in lenalidomide-refractory multiple myeloma. *N. Engl. J. Med.* **389**, 335–347 (2023).

53. P. Moreau, A. L. Garfall, N. W. C. J. van de Donk, H. Nahi, J. F. San-Miguel, A. Oriol, A. K. Nooka, T. Martin, L. Rosinol, A. Chari, L. Karlin, L. Benboubker, M.-V. Mateos, N. Bahlis, R. Popat, B. Besemer, J. Martínez-López, S. Sidana, M. Delforge, L. Pei, D. Trancucci, R. Verona, S. Girgis, S. X. W. Lin, Y. Olyslager, M. Jaffe, C. Uhlar, T. Stephenson, R. Van Rampelbergh, A. Banerjee, J. D. Goldberg, R. Kobos, A. Krishnan, S. Z. Usmani, Teclistamab in relapsed or refractory multiple myeloma. *N. Engl. J. Med.* **387**, 495–505 (2022).

54. A. M. Lesokhin, M. H. Tomasson, B. Arnulf, N. J. Bahlis, H. Miles Prince, R. Niesvizky, P. Rodriguez-Otero, J. Martinez-Lopez, G. Koehne, C. Touzeau, Y. Jethava, H. Quach, J. Depaus, H. Yokoyama, A. E. Gabayan, D. A. Stevens, A. K. Nooka, S. Manier, N. Raje, S. Iida, M.-S. Raab, E. Searle, E. Leip, S. T. Sullivan, U. Conte, M. Elmeliegy, A. Czibere, A. Viqueira, M. Mohty, Elranatamab in relapsed or refractory multiple myeloma: Phase 2 MagnetisMM-3 trial results. *Nat. Med.* **29**, 2259–2267 (2023).

55. E. Reisinger, L. Genthner, J. Kerssemakers, P. Kensche, S. Borufka, A. Jugold, A. Kling, M. Prinz, I. Scholz, G. Zipprich, R. Eils, C. Lawerenz, J. Eils, OTP: An automated system for managing and processing NGS data. *J. Biotechnol.* **261**, 53–62 (2017).

56. K. A. Kleinheinz, I. Bludau, D. Hübschmann, M. Heinold, P. Kensche, Z. Gu, C. López, M. Hummel, W. Klapper, P. Möller, I. Vater, R. Wagener, ICGC MMML-Seq project, B. Brors, R. Siebert, R. Eils, M. Schlesner, ACEseq—Allele-specific copy number estimation from whole genome sequencing and its application in heterogeneity and integrative analyses of cancer. bioRxiv 210807 [Preprint] (2017). https://doi.org/10.1101/210807.

57. P. Danecek, J. K. Bonfield, J. Liddle, J. Marshall, V. Ohan, M. O. Pollard, A. Whitwham, T. Keane, S. A. McCarthy, R. M. Davies, H. Li, Twelve years of SAMtools and BCFtools. *Gigascience* **10**, giab008 (2021).

58. The ICGC/TCGA Pan-Cancer Analysis of Whole Genomes Consortium, Pan-cancer analysis of whole genomes. *Nature* **578**, 82–93 (2020).

59. J. T. Robinson, H. Thorvaldsdóttir, W. Winckler, M. Guttman, E. S. Lander, G. Getz, J. P. Mesirov, Integrative genomics viewer. *Nat. Biotechnol.* **29**, 24–26 (2011).

60. E. K. Barnell, P. Ronning, K. M. Campbell, K. Krysiak, B. J. Ainscough, L. M. Sheta, S. P. Pema, A. D. Schmidt, M. Richters, K. C. Cotto, A. M. Danos, C. Ramirez, Z. L. Skidmore, N. C. Spies, J. Hundal, M. S. Sediqzad, J. Kunisaki, F. Gomez, L. Trani, M. Matlock, A. H. Wagner, S. J. Swamidass, M. Griffith, O. L. Griffith, Standard operating procedure for somatic variant refinement of sequencing data with paired tumor and normal samples. *Genet. Med.* **21**, 972–981 (2019).

61. F. Rivest, D. Eroglu, B. Pelz, J. Kowal, A. Kehren, V. Navikas, M. G. Procopio, P. Bordignon, E. Pérès, M. Ammann, E. Dorel, S. Scalmazzi, L. Bruno, G. Campargue, G. Casqueiro, L. Arn, J. Fischer, S. Brajkovic, P. Joris, M. Cassano, D. Dupouy, Fully automated sequential immunofluorescence (seqIF) for hyperplex spatial proteomics. *Sci. Rep.* **13**, 16994 (2023).

62. P. J. Stephens, P. S. Tarpey, H. Davies, P. Van Loo, C. Greenman, D. C. Wedge, S. Nik-Zainal, S. Martin, I. Varela, G. R. Bignell, L. R. Yates, E. Papaemmanuil, D. Beare, A. Butler, A. Cheverton, J. Gamble, J. Hinton, M. Jia, A. Jayakumar, D. Jones, C. Latimer, K. W. Lau, S. McLaren, D. J. McBride, A. Menzies, L. Mudie, K. Raine, R. Rad, M. S. Chapman, J. Teague, D. Easton, A. Langerød, Oslo Breast Cancer Consortium (OSBREAC), M. T. M. Lee, C.-Y. Shen, B. T. K. Tee, B. W. Huimin, A. Broeks, A. C. Vargas, G. Turashvili, J. Martens, A. Fatima, P. Miron, S.-F. Chin, G. Thomas, S. Boyault, O. Mariani, S. R. Lakhani, M. van de Vijver, L. van 't Veer, J. Foekens, C. Desmedt, C. Sotiriou, A. Tutt, C. Caldas, J. S. Reis-Filho, S. A. J. R. Aparicio, A. V. Salomon, A.-L. Børresen-Dale, A. L. Richardson, P. J. Campbell, P. A. Futreal, M. R. Stratton, The landscape of cancer genes and mutational processes in breast cancer. *Nature* **486**, 400–404 (2012).

63. M. Gerstung, C. Jolly, I. Leshchiner, S. C. Dentro, S. Gonzalez, D. Rosebrock, T. J. Mitchell, Y. Rubanova, P. Anur, K. Yu, M. Tarabichi, A. Deshwar, J. Wintersinger, K. Kleinheinz, I. Vázquez-García, K. Haase, L. Jerman, S. Sengupta, G. Macintyre, S. Malikic, N. Donmez, D. G. Livitz, M. Cmero, J. Demeulemeester, S. Schumacher, Y. Fan, X. Yao, J. Lee, M. Schlesner, P. C. Boutros, D. D. Bowtell, H. Zhu, G. Getz, M. Imielinski, R. Beroukhim, S. C. Sahinalp, Y. Ji, M. Peifer, F. Markowetz, V. Mustonen, K. Yuan, W. Wang, Q. D. Morris, PCAWG Evolution & Heterogeneity Working Group, P.T. Spellman, D. C. Wedge, P. Van Loo, PCAWG Consortium, The evolutionary history of 2,658 cancers. *Nature* **578**, 122–128 (2020).

64. F. Maura, A. R. Rajanna, B. Ziccheddu, A. M. Poos, A. Derkach, K. Maclachlan, M. Durante, B. Diamond, M. Papadimitriou, F. Davies, E. M. Boyle, B. Walker, M. Hultcrantz, A. Silva, O. Hampton, J. K. Teer, E. M. Siegel, N. Bolli, G. H. Jackson, M. Kaiser, C. Pawlyn, G. Cook, D. Kazandjian, C. Stein, M. Chesi, L. Bergsagel, E. K. Mai, H. Goldschmidt, K. C. Weisel, R. Fenk, M. S. Raab, F. Van Rhee, S. Usmani, K. H. Shain, N. Weinhold, G. Morgan, O. Landgren, Genomic classification and individualized prognosis in multiple myeloma. *J. Clin. Oncol.* **42**, 1229–1240 (2024).

65. M. Andreatta, A. J. Berenstein, S. J. Carmona, scGate: Marker-based purification of cell types from heterogeneous single-cell RNA-seq datasets. *Bioinformatics* **38**, 2642–2644 (2022).

66. Y. Huang, D. J. McCarthy, O. Stegle, Vireo: Bayesian demultiplexing of pooled single-cell RNA-seq data without genotype reference. *Genome Biol.* **20**, 273 (2019).

67. P.-L. Germain, A. Lun, C. Garcia Meixide, W. Macnair, M. D. Robinson, Doublet identification in single-cell sequencing data using scDblFinder. *F1000Res.* **10**, 979 (2021).

68. C. Hafemeister, R. Satija, Normalization and variance stabilization of single-cell RNA-seq data using regularized negative binomial regression. *Genome Biol.* **20**, 296 (2019).

69. E. Becht, L. McInnes, J. Healy, C.-A. Dutertre, I. W. H. Kwok, L. G. Ng, F. Ginhoux, E. W. Newell, Dimensionality reduction for visualizing single-cell data using UMAP. *Nat. Biotechnol.* **37**, 38–44 (2019).

70. S. Tietscher, J. Wagner, T. Anzeneder, C. Langwieder, M. Rees, B. Sobottka, N. de Souza, B. Bodenmiller, A comprehensive single-cell map of T cell exhaustion-associated immune environments in human breast cancer. *Nat. Commun.* **14**, 98 (2023).

71. N. Borcherding, N. L. Bormann, G. Kraus, scRepertoire: An R-based toolkit for single-cell immune receptor analysis. *F1000Res.* **9**, 47 (2020).

72. D. V. Bagaev, R. M. A. Vroomans, J. Samir, U. Stervbo, C. Rius, G. Dolton, A. Greenshields-Watson, M. Attaf, E. S. Egorov, I. V. Zvyagin, N. Babel, D. K. Cole, A. J. Godkin, A. K. Sewell, C. Kesmir, D. M. Chudakov, F. Luciani, M. Shugay, VDJdb in 2019: Database extension, new analysis infrastructure and a T-cell receptor motif compendium. *Nucleic Acids Res.* **48**, D1057–D1062 (2020).

73. N. Tickotsky, T. Sagiv, J. Prilusky, E. Shifrut, N. Friedman, McPAS-TCR: A manually curated catalogue of pathology-associated T cell receptor sequences. *Bioinformatics* **33**, 2924–2929 (2017).

74. D. Schapiro, A. Sokolov, C. Yapp, Y.-A. Chen, J. L. Muhlich, J. Hess, A. L. Creason, A. J. Nirmal, G. J. Baker, M. K. Nariya, J.-R. Lin, Z. Maliga, C. A. Jacobson, M. W. Hodgman, J. Ruokonen, S. L. Farhi, D. Abbondanza, E. T. McKinley, D. Persson, C. Betts, S. Sivagnanam, A. Regev, J. Goecks, R. J. Coffey, L. M. Coussens, S. Santagata, P. K. Sorger, MCMICRO: A scalable, modular image-processing pipeline for multiplexed tissue imaging. *Nat. Methods* **19**, 311–315 (2022).

75. N. F. Greenwald, G. Miller, E. Moen, A. Kong, A. Kagel, T. Dougherty, C. C. Fullaway, B. J. McIntosh, K. X. Leow, M. S. Schwartz, C. Pavelchek, S. Cui, I. Camplisson, O. Bar-Tal, J. Singh, M. Fong, G. Chaudhry, Z. Abraham, J. Moseley, S. Warshawsky, E. Soon, S. Greenbaum, T. Risom, T. Hollmann, S. C. Bendall, L. Keren, W. Graf, M. Angelo, D. Van Valen, Whole-cell segmentation of tissue images with human-level performance using large-scale data annotation and deep learning. *Nat. Biotechnol.* **40**, 555–565 (2022).

76. F. A. Wolf, P. Angerer, F. J. Theis, SCANPY: Large-scale single-cell gene expression data analysis. *Genome Biol.* **19**, 15 (2018).

77. J. W. Hickey, Y. Tan, G. P. Nolan, Y. Goltsev, Strategies for accurate cell type identification in CODEX multiplexed imaging data. *Front. Immunol.* **12**, 727626 (2021).

78. T. Roider, M. A. Baertsch, D. Fitzgerald, H. Vöhringer, B. J. Brinkmann, F. Czernilofsky, M. Knoll, L. Lladó-Cid, A. Mathioudaki, B. Faßbender, M. Herbon, T. Lautwein, P.-M. Bruch, N. Liebers, C. M. Schürch, V. Passerini, M. Seifert, A. Brobeil, G. Mechtersheimer, C. Müller-Tidow, O. Weigert, M. Seiffert, G. P. Nolan, W. Huber, S. Dietrich, Multimodal and spatially resolved profiling identifies distinct patterns of T cell infiltration in nodal B cell lymphoma entities. *Nat. Cell Biol.* **26**, 478–489 (2024).

79. A. J. Nirmal, P. K. Sorger, SCIMAP: A python toolkit for integrated spatial analysis of multiplexed imaging data. *J. Open Source Softw.* **9**, 6604 (2024).